

Fast Registration Based on Noisy Planes With Unknown Correspondences for 3-D Mapping

Kaustubh Pathak, *Member, IEEE*, Andreas Birk, *Member, IEEE*, Narūnas Vaškevičius, and Jann Poppinga

Abstract—We present a robot-pose-registration algorithm, which is entirely based on large planar-surface patches extracted from point clouds sampled from a three-dimensional (3-D) sensor. This approach offers an alternative to the traditional point-to-point iterative-closest-point (ICP) algorithm, its point-to-plane variant, as well as newer grid-based algorithms, such as the 3-D normal distribution transform (NDT). The simpler case of known plane correspondences is tackled first by deriving expressions for least-squares pose estimation considering plane-parameter uncertainty computed during plane extraction. Closed-form expressions for covariances are also derived. To round-off the solution, we present a new algorithm, which is called minimally uncertain maximal consensus (MUMC), to determine the unknown plane correspondences by maximizing geometric consistency by minimizing the uncertainty volume in configuration space. Experimental results from three 3-D sensors, viz., Swiss-Ranger, University of South Florida Odetics Laser Detection and Ranging, and an actuated SICK S300, are given. The first two have low fields of view (FOV) and moderate ranges, while the third has a much bigger FOV and range. Experimental results show that this approach is not only more robust than point- or grid-based approaches in plane-rich environments, but it is also faster, requires significantly less memory, and offers a less-cluttered planar-patches-based visualization.

Index Terms—Localization, mapping, planes-based pose registration, sensor fusion, simultaneous localization and mapping (SLAM).

I. INTRODUCTION

ENCOURAGED by the success of 2-D simultaneous localization and mapping (SLAM) [1], there have been many recent attempts [2]–[6] to extend the methodology to 3-D. Since onboard 3-D odometry is usually lacking or inadequate, an essential part of the mapping procedure finds the relative pose offset of the robot between two successive range sensor samples using scan matching. Typical 3-D sensors are laser-range finders (LRFs), which are mounted on a rotating platform [3], and time-of-flight sensors, like the Swiss-Ranger (SR) [7]. These sensors provide a 3-D-range scan as a “point cloud” of noisy

spatial coordinates, which number typically between 10^4 and 10^6 .

The most commonly used scan-matching algorithm is the point-to-point (P-P) iterative closest-point (ICP) [8], which works with the points directly and, hence, assumes no specific structure in the environment. A recent dissertation [9, p. 4] notes that “*up to now, all approaches successfully applied to 3-D SLAM are based on the ICP algorithm.*” There also exists a point-to-plane (P-L) version of ICP [10], [11]. Its cost function differs from that of P-P ICP in that it minimizes error along local normals. This increases its robustness to outliers, although no closed-form solution exists for the minimization of its cost function. One alternative to ICP is the 3-D normal-distribution transform (3-D-NDT) [5], which uses a combination of normal distributions defined on an occupancy-grid-like structure. This gives a piecewise smooth representation of the point cloud on which standard iterative numerical optimization methods are applied to obtain the registration.

If the environment to be mapped has some structure, e.g., if it is made up of many planar surface patches, then a map based on plane segments offers many advantages in terms of storage requirements, computational efficiency, semantic classification of surface features, and ease of visualization. Furthermore, these features can be easily embedded in an extended Kalman filter (EKF) EKF-SLAM framework [12]. As in [4], we utilize planar-surface patches. However, our approach obviates the ICP step necessary for the pose-change prediction in their work. The basic steps of the algorithms are compared in Fig. 1. Combining plane-correspondence determination and pose registration in one step and removal of ICP leads to savings in computation time and an increase in robustness. In fact, most of the previous 3-D-mapping approaches have been offline due to the excessive time required by ICP. With the new approach presented in this paper, the pose registration is fast enough relative to the per sample data-acquisition time of the sensor, to be practicable for mapping in a stop-and-go fashion, with relatively large movements of the robot between samples. This contrasts with approaches [13], [14] wherein the sampling is so fast that instantaneous kinematic information may be utilized to aid registration. This also holds for early work on motion determination using camera images utilizing properties of planes in projective geometry [15].

In this paper, we focus on the steps marked with a box in Fig. 1 as they are the core elements for 3-D mapping. The SLAM step can be, for example, the same as in [4], i.e., the well-known EKF algorithm, and is outside the scope of this paper. Nevertheless, we have already embedded the approach presented here in a SLAM framework using pose graphs [16]. The resulting 3-D maps are presented at <http://robotics.jacobs-university.de/>

Manuscript received August 28, 2008; revised May 8, 2009 and November 19, 2009; accepted February 3, 2010. Date of publication March 15, 2010; date of current version June 9, 2010. This paper was recommended for publication by Associate Editor S. Roumeliotis and Editor L. Parker upon evaluation of the reviewers' comments. This work was supported by the German Research Foundation. This paper was presented in part at the 2009 IEEE/Robotics Society of Japan International Conference on Intelligent Robots and Systems, St. Louis, MO.

The authors are with the Department of Electrical Engineering and Computer Science, Jacobs University Bremen, Bremen 28751, Germany (e-mail: k.pathak@jacobs-university.de; a.birk@jacobs-university.de; n.vaskevicius@jacobs-university.de; j.poppinga@jacobs-university.de).

Color versions of one or more of the figures in this paper are available online at <http://ieeexplore.ieee.org>.

Digital Object Identifier 10.1109/TRO.2010.2042989

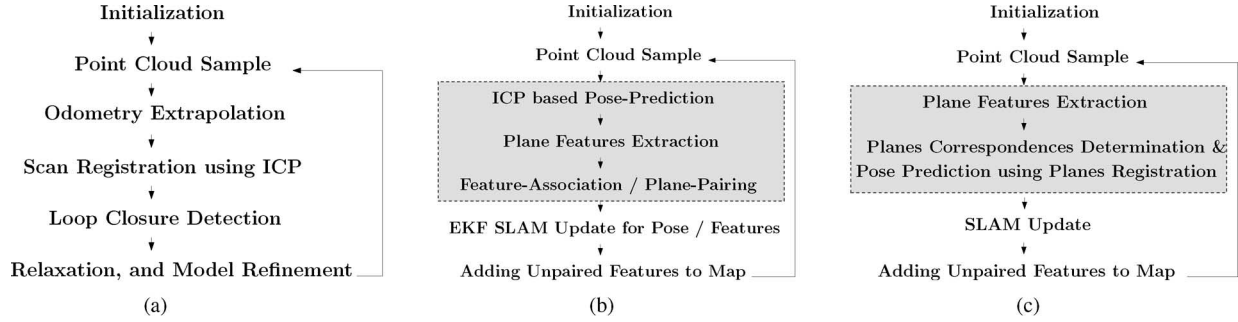


Fig. 1. Comparison of algorithm structures. The ICP step in the Weingarten *et al.* approach has been removed in our approach. (a) Approach of Nüchter *et al.* [6]. (b) Approach of Weingarten [9]. (c) Approach presented in this paper.

projects/3Dmap. For the planes-extraction step and uncertainty analysis, see [17] and [18].

Our approach falls into the category of *large* 3-D surface-patches-based pose estimation without prior knowledge of correspondences. The work by Kohlhepp *et al.* [2], [19], [20] is most related to ours. Surfaces are extracted from range images in [19], which are obtained by a rotating LRF and registered together. A local module determines the correspondences and computes transforms, and a global module detects loop-closure and distributes uncertainty using an elastic graph. For this paper, only the local module is relevant, which is discussed again in [20]. Similar to Section II-C of this paper, their approach uses surface-patch directions to compute the rotation between successive views. However, no mention is made in their work of using the uncertainties in the extracted surface parameters. To estimate translation, they resort back to point features, which is essentially the same as ICP. By contrast, this paper uses only planar patches and does not return to the domain of points—even translation is obtained using planes. This allows for the detection of dominant directions of uncertainties, as detailed in Section II-D. Note that the uncertainties are absolutely necessary to make the registration usable for proper 3-D SLAM. Furthermore, many heuristic measures to estimate correspondences between features, in particular, the ground, across views are discussed in [20]. By contrast, the plane-correspondence algorithm, which is presented by us, does not give any special status to the ground. In our view, their work—although substantial—describes the mathematical machinery insufficiently: It neither computes the uncertainties in feature parameters in the extracted features nor discusses how these uncertainties affect the final-pose estimation.

A very comprehensive discussion on finding correspondences between two sets of planar or quadratic patches using attribute graphs is found in [2], where similarity metrics were formulated based on several attributes, like shape factor, area ratio, curvature histogram, intersurface relations, etc., and a bounded tree search was performed to give a set of correspondences that maximized the metric. The result is refined using an evolutionary algorithm, which is computation-time intensive. In contrast, we use only planar patches, and an algorithm is described that maximizes the overall geometric consistency within a search space to determine correspondences between planes. The search space is pruned using criteria such as overlap, size similarity,

and agreement with odometry, if available. For all these tests, only the plane-parameter covariance matrix is employed, without the need to refer back to the original point cloud. There is, of course, the option to also use additional attributes, like intensity and color, to make the correspondence-finding step more reliable. The use of geometric constraints for planar-surface matching has been discussed in [21], in which most constraints are formulated as algebraic inequalities *without* employing covariances of plane parameters computed during extraction. Only theoretical and simulation results in a geometric reasoning network were provided without any experimental validation. The general concept of interpretation trees for correspondence finding was introduced in [22], which was later used in [23] to register planar patches using filters based on area, normal direction, and centroids. The latter work, however, suffers from several following shortcomings.

- 1) Their approach is only applicable to *complete* planar patches, i.e., if a patch is only partially visible due to occlusion, it cannot be matched.
- 2) The actual computation of the registration has not been worked out, and it is claimed that only two correspondences are enough for registration. As we show in Section II, at least three nonparallel-plane correspondences are needed if completeness of patches is not assumed.
- 3) As experimental evidence, their paper shows the matching of a *single* scan pair.
- 4) Again, the covariances of plane parameters were not computed or used. Similarly, the covariance of the registration was not computed.

In our work, the covariance of the plane parameters, as well as the covariance of the registration solution, play a central role in the matching. Another heuristic iterative ICP-like matching algorithm for small planar patches was developed in [24]. They extract only *small local patches* and apply an ICP-like algorithm on these patches—no consensus is built, but several empirical measures are used. Translation is computed using the overlap method similar to [23], which is only valid when there is no occlusion. Correlation in the Fourier domain of *local* surface normals is used in [25] for registration.

Another line of correspondence-determination approaches uses random sample consensus (RANSAC) [26], which was employed in [27] in combination with a Huber kernel to match

2-D light detection and ranging (LIDAR) samples. Their algorithm works in 2-D and finds the biggest corresponding points set that verifies the interpoint distance-rigidity constraint. Since we also use the idea of “consensus” in our approach, it is similar in spirit to RANSAC, albeit with two important differences: No random sampling is involved, and more importantly, the solution is not only based solely on consensus maximization but also uses the uncertainty volume of potential registration solutions.

A. Problem Formulation

In this subsection, we formulate the problem of plane-matching-based registration. Two sets of planes are given, which are extracted from two successive views of a 3-D sensor, which is rigidly mounted on a mobile robot. From these planes, we would like to estimate the change in position and orientation of the sensor between the samples. The problem can be formulated in the following two scenarios with increasing levels of difficulty.

- 1) Both views have the same planes, and the correspondences between planes across the views is also given.
- 2) The two views have only some planes, which overlap, i.e., some planes go out of view, and new planes, which were not previously visible, come into view. Which planes are overlapping and what their correspondences are is not known.

In this paper, we address both cases mentioned above. We start out by deriving a closed-form solution for the simplest case of known correspondences in Section II. We also derive the covariances for the computed registration. This allows us to compute an uncertainty metric, which can be used to measure the geometrical consistency of any assigned correspondences.

The most general case of unknown correspondences is handled in Section III, where we propose a new algorithm called the minimally uncertain maximal consensus (MUMC). Some results of applying MUMC to real sensor data are presented in Section IV, which also provide a comparison with P-P and P-L ICP and 3-D NDT. Finally, the paper is concluded in Section V.

II. PLANES WITH KNOWN CORRESPONDENCES

In this paper, the following notations have been used:

- $v, \mathbf{v}, \hat{\mathbf{v}}$ a scalar, a vector, and a unit vector;
- \mathbf{M}, \mathbf{M}^+ a matrix, its Moore–Penrose pseudoinverse;
- $|\mathbf{M}|, |\mathbf{M}|_+$ the determinant and the pseudodeterminant;
- $\check{\mathbf{q}}, \check{\mathbf{q}}^*$ a quaternion and its conjugate;
- $\mathbf{u} \cdot \mathbf{v}, \check{\mathbf{p}} \diamond \check{\mathbf{q}}$ vector dot product and quaternion product.

The pseudodeterminant of a matrix is simply the product of its nonzero eigenvalues. Additionally, for quantities resolved in different frames, we use the left superscript/subscript notation of [28].

A plane $\mathcal{P}(\hat{\mathbf{m}}, \rho)$ is given by the equation $\hat{\mathbf{m}} \cdot \mathbf{p} = \rho$, where ρ is the signed distance from the origin in the direction of the unit plane normal $\hat{\mathbf{m}}$. We see that $\mathcal{P}(\hat{\mathbf{m}}, \rho) \equiv \mathcal{P}(-\hat{\mathbf{m}}, -\rho)$. To achieve a consistent sign convention, we define planes as

$\mathcal{P}(\hat{\mathbf{n}}, d)$, where, $d \triangleq |\rho| \geq 0$, and $\hat{\mathbf{n}} \triangleq \sigma(\rho) \hat{\mathbf{m}}$, where $\sigma(\rho) = -1$ if $\rho < 0$ and $+1$, otherwise. If $\rho = 0$, then we choose the maximum component of $\hat{\mathbf{n}}$ to be positive. The latter case is unlikely to occur, in practice, in the sensor frame, because such a plane, which is parallel to the line of sight of the range sensor, is unlikely to be detected by it.

An indexed set ${}^k\mathcal{P}$ of planar patches is extracted [17] from a point cloud associated with the k th robot frame \mathcal{F}_k . Apart from the planar patch's $\hat{\mathbf{n}}$ and d parameters, the extraction procedure also gives [18] their 4×4 covariance matrix \mathbf{C} . Thus, ${}^k\mathcal{P}$ is an ordered set of triplets given by

$${}^k\mathcal{P} \triangleq \{ {}^k\mathcal{P}_i \langle {}^k\hat{\mathbf{n}}_i, {}^k d_i, {}^k\mathbf{C}_i \rangle, i = 1, \dots, N_k \}. \quad (1)$$

Additional information, like bounding boxes or the outlines of the patches, may be available but is not needed in our formulation.

For registration, we consider two robot frames: a left one, which is denoted as \mathcal{F}_ℓ , with origin \mathcal{O}_ℓ from which the indexed plane set ${}^\ell\mathcal{P}$ is observed, and a right one, which is denoted as \mathcal{F}_r , with origin \mathcal{O}_r , from which the indexed plane set ${}^r\mathcal{P}$ is observed. The equations of the planes are given by

$${}^\ell\hat{\mathbf{n}}_i \cdot {}^\ell\mathbf{p} = {}^\ell d_i, \quad {}^r\hat{\mathbf{n}}_i \cdot {}^r\mathbf{p} = {}^r d_i. \quad (2)$$

At this juncture, it is assumed that the correspondence problem has already been solved, i.e., the planes at the corresponding index i in the two sets have been found to represent the same physical plane.

If the robot moves from \mathcal{F}_ℓ to \mathcal{F}_r , and observes the coordinates of the same physical point as ${}^\ell\mathbf{p}$ and ${}^r\mathbf{p}$, respectively, these coordinates are related by [28]

$${}^\ell\mathbf{p} = {}^\ell\mathbf{R} {}^r\mathbf{p} + {}^\ell\mathbf{t} \quad (3)$$

where the translation ${}^\ell\mathbf{t} \triangleq \overrightarrow{\mathcal{O}_\ell \mathcal{O}_r}$, resolved in \mathcal{F}_ℓ .

The registration problem now consists of estimating ${}^\ell\mathbf{R}$ and ${}^\ell\mathbf{t}$. Substituting (3) into (2) and comparing coefficients, we have

$${}^\ell\hat{\mathbf{n}}_i = {}^\ell\mathbf{R} {}^r\hat{\mathbf{n}}_i \quad (4a)$$

$${}^\ell\hat{\mathbf{n}}_i \cdot {}^\ell\mathbf{t} = {}^\ell d_i - {}^r d_i. \quad (4b)$$

We would not have been able to write these equations had we not enforced the aforementioned sign convention for both sets of planes.

1) *Plane-Parameter Covariance Matrix*: For details on the computation of the plane-parameter covariance matrix, see the authors' previous work on the extraction of planes from noisy point-cloud data; Poppinga *et al.* [17] described the extraction of planes and their polygonal boundaries, and Pathak *et al.* [18] dealt with the proper calculation of the related uncertainties. The main results are summarized in Appendix A. The 4×4 plane covariance matrix can be partitioned as

$$\mathbf{C} = \begin{bmatrix} \mathbf{C}_{\hat{\mathbf{n}}\hat{\mathbf{n}}} & \mathbf{C}_{\hat{\mathbf{n}}d} \\ \mathbf{C}_{\hat{\mathbf{n}}d}^T & \mathbf{C}_{dd} \end{bmatrix}. \quad (5)$$

Since $\|\hat{\mathbf{n}}\| = 1$, there is uncertainty only in three independent directions. Therefore, this matrix is rank-deficient [29] with rank

3. This, however, does not pose a problem if we interpret results properly. As suggested in [30], we use the Moore–Penrose inverse to obtain the inverse of the covariance matrix (i.e., the information matrix). Let the eigenvalue decomposition of the positive semidefinite \mathbf{C} be

$$\mathbf{C} = \sum_{i=1}^3 \sigma_i^2 \hat{\mathbf{u}}_i \hat{\mathbf{u}}_i^\top, \quad \sigma_1^2 \geq \sigma_2^2 \geq \sigma_3^2, \quad \sigma_4^2 = 0. \quad (6)$$

We define the following quantities based on the Moore–Penrose inverse:

$$\mathbf{C}^+ \triangleq \sum_{i=1}^3 \frac{1}{\sigma_i^2} \hat{\mathbf{u}}_i \hat{\mathbf{u}}_i^\top, \quad \mathbf{H} \triangleq -\mathbf{C}^+ \quad (7)$$

$$|\mathbf{C}|_+ \triangleq \sigma_1^2 \sigma_2^2 \sigma_3^2, \quad |\mathbf{C}^+|_+ \triangleq |\mathbf{C}|_+^{-1}. \quad (8)$$

The matrix \mathbf{H} is the Hessian of the log-likelihood function with which the covariance can be estimated, as given in [31]. In our formulation, the Hessian plays a central role because it, rather than the covariance, is estimated directly in our plane-extraction step [17], [18]. Defining

$$\boldsymbol{\nu} \triangleq [\hat{\mathbf{n}}^\top \ d]^\top \quad (9a)$$

$${}^r \mathbf{T} \triangleq \begin{bmatrix} {}^r \mathbf{R}^\top & \mathbf{0}_{3 \times 1} \\ -{}^r \mathbf{t}^\top & 1 \end{bmatrix}, \text{ we get, } {}^r \boldsymbol{\nu} = {}^r \mathbf{T} {}^\ell \boldsymbol{\nu}. \quad (9b)$$

The maximum-likelihood registration is then found by doing the following extremization:

$$\begin{aligned} \min_{{}^r \mathbf{T}} \zeta_T &\triangleq \frac{1}{2} \sum_{i=1}^N ({}^r \boldsymbol{\nu}_i - {}^r \mathbf{T} {}^\ell \boldsymbol{\nu}_i)^\top \mathbf{C}_i^+ ({}^r \boldsymbol{\nu}_i - {}^r \mathbf{T} {}^\ell \boldsymbol{\nu}_i) \\ &+ \frac{1}{2} \sum_{i=1}^N \log |\mathbf{C}_i|_+, \text{ where} \end{aligned} \quad (10a)$$

$$\mathbf{C}_i \triangleq {}^r \mathbf{C}_i + {}^r \mathbf{T} {}^\ell \mathbf{C}_i {}^\ell \mathbf{T}^\top. \quad (10b)$$

Due to the coupling of rotation and translation estimation, this is hard to tackle analytically. Iterative numerical optimization could be employed—however, in this paper, we are looking for closed-form solutions, which can be employed for online planes-based mapping. Therefore, we look for fast-to-compute alternatives using decoupling of covariances and application of least squares (LSs).

A. Plane-Parametrization Choice

Several plane parametrizations have been listed in [9, p. 29]. Only the $\hat{\mathbf{n}}, d$ parameterization, which is used in this paper, is free of singularities and can represent all possible planes. The 4×4 covariance matrix of this representation is, however, singular. This does not actually represent any difficulty and singular covariance matrices are used routinely in classic works in Computer Vision like [30]. In our approach [18], we go one step further and *exploit* this singularity to place the plane’s parameters exactly in the null space of its covariance.

An inefficient work-around is used in [9]. They first use the $\hat{\mathbf{n}}, d$ plane parameterization for plane-fitting using principal-

component analysis, then rotate all the points such that the plane’s normal becomes the $\hat{\mathbf{z}}$ -axis, and then refit the plane using a different model $z = ax + by + d$ using LSs to compute a 3×3 covariance matrix for a, b , and d . This is particularly wasteful because of the plane-fitting problem being effectively solved twice. Although the 3×3 covariance matrix is nonsingular, the parameterization on which it is based is local to the plane and cannot represent all planes. Hence, we are of the opinion that the singularity of the covariance matrix should not be avoided because it makes the underlying topology of the rotation group $SO(2)$ explicit (or $SO(3)$ later for the unit quaternions).

B. Decoupling the Covariances

To be able to use the nicely decoupled equations [see (4)] to determine rotation and translation separately, we need to estimate the total uncertainty in $\hat{\mathbf{n}}$ by marginalizing, i.e., integrating out the effect of d and *vice versa*. The details of this decoupling are shown in Appendix B. This gives us two decoupled covariances: a scalar variance \mathbf{D}_{dd} for d , and a 3×3 covariance $\mathbf{D}_{\hat{\mathbf{n}}\hat{\mathbf{n}}}$ for $\hat{\mathbf{n}}$.

Armed with the above expressions for decoupled covariances, we can go back to the decoupled equations [see (4)] to find the registration. Henceforth, in this paper, we will mostly use these *decoupled* covariances, which are denoted by \mathbf{D} , as given in (58) and (61) for the plane-parameter covariances. When the original *coupled* covariances are needed, e.g., in Section III-A1–A4, we will use the symbol \mathbf{C} .

C. Least-Squares Rotation After Decoupling and Assuming Isotropic Uncertainties

In this section, we derive a solution to compute ${}^\ell \mathbf{R}$. Considering first the uncertainty for any given normal to be directionally uniform/isotropic, but varying only in its magnitude, leads to a log-likelihood function, which is straightforward to analyze. We define the rotational residual for the i th correspondence as

$$\mathbf{s}_i \triangleq {}^\ell \hat{\mathbf{n}}_i - {}^\ell \mathbf{R} {}^r \hat{\mathbf{n}}_i. \quad (11)$$

Due to the isotropy approximation, it is assumed to be normally distributed with mean $\mathbf{0}$ and covariance $w_i^{-1} \mathbf{I}_3$, where w_i are weights that are inversely proportional to a measure of rotational uncertainty. Using the property that trace is unitary invariant, the weights are selected as

$$w_i^{-1} = \text{trace}({}^\ell \mathbf{D}_{i,\hat{\mathbf{n}}\hat{\mathbf{n}}} + {}^\ell \mathbf{R} {}^r \mathbf{D}_{i,\hat{\mathbf{n}}\hat{\mathbf{n}}} {}^\ell \mathbf{R}^\top) \quad (12)$$

$$= \text{trace}({}^\ell \mathbf{D}_{i,\hat{\mathbf{n}}\hat{\mathbf{n}}} + {}^r \mathbf{D}_{i,\hat{\mathbf{n}}\hat{\mathbf{n}}}). \quad (13)$$

We, therefore, need to maximize the log-likelihood function as follows:

$$\max_{{}^\ell \mathbf{R}} \zeta_r = -\frac{1}{2} \sum_{i=1}^N w_i \|\mathbf{s}_i\|^2 \quad (14)$$

$$\equiv \text{constant} + \sum_{i=1}^N w_i {}^\ell \hat{\mathbf{n}}_i \cdot ({}^\ell \mathbf{R} {}^r \hat{\mathbf{n}}_i). \quad (15)$$

There are essentially two ways to solve this—by using quaternions [32, Sec. IV] and by using singular value decomposition

(SVD) [30]. In the context of satellite-attitude estimation using a star tracker, this problem is called the Wahba's problem [33], and the quaternion-based solution is called the Davenport's q-method.

Here, we employ the quaternion-based approach, as it leads to an easier formulation of the anisotropic uncertainty version in the next section. The solution involves representing the rotation operator ${}^\ell_r \mathbf{R}$ using a unit quaternion ${}^\ell_r \mathbf{q}$. The unit normal vector $\hat{\mathbf{n}}$ now becomes the purely imaginary quaternion $\hat{\mathbf{n}} = [0 \quad \hat{\mathbf{n}}^\top]^\top$. Then, (4a) can be rewritten as ${}^\ell \hat{\mathbf{n}}_i = {}^\ell_r \mathbf{q} \diamond {}^r \hat{\mathbf{n}}_i \diamond {}^\ell_r \mathbf{q}^*$.

After dropping the constant, (15) can be written as

$$\begin{aligned} \max_{{}^\ell_r \mathbf{q}} \zeta_r &= \sum_{i=1}^N w_i ({}^\ell_r \mathbf{q} \diamond {}^r \hat{\mathbf{n}}_i \diamond {}^\ell_r \mathbf{q}^*) \cdot {}^\ell \hat{\mathbf{n}}_i \\ &= {}^\ell_r \mathbf{q}^\top \left(\sum_{i=1}^N w_i \bar{\Psi}^\top ({}^r \hat{\mathbf{n}}_i) \Psi ({}^\ell \hat{\mathbf{n}}_i) \right) {}^\ell_r \mathbf{q} \\ &\triangleq {}^\ell_r \mathbf{q}^\top \mathbf{K} {}^\ell_r \mathbf{q} \end{aligned} \quad (16)$$

where the following definitions have been used. Letting the quaternion $\check{\mathbf{p}} \triangleq [p_0 \quad p_x \quad p_y \quad p_z]^\top \triangleq [p_0 \quad \mathbf{p}^\top]^\top$, then

$$\check{\mathbf{p}} \diamond \check{\mathbf{q}} \triangleq \Psi(\check{\mathbf{p}})\check{\mathbf{q}} \triangleq \begin{bmatrix} p_0 & -\mathbf{p}^\top \\ \mathbf{p} & p_0 \mathbf{I}_3 + \mathbf{p} \times \mathbf{I}_3 \end{bmatrix} \check{\mathbf{q}} \quad (17a)$$

$$\check{\mathbf{q}} \diamond \check{\mathbf{p}} \triangleq \bar{\Psi}(\check{\mathbf{p}})\check{\mathbf{q}} \triangleq \begin{bmatrix} p_0 & -\mathbf{p}^\top \\ \mathbf{p} & p_0 \mathbf{I}_3 - \mathbf{p} \times \mathbf{I}_3 \end{bmatrix} \check{\mathbf{q}}. \quad (17b)$$

$\mathbf{p} \times \mathbf{I}_3$ is the cross-product skew-symmetric matrix [30]. The maximum of ζ_r is then achieved at the 4×1 unit Eigenvector ${}^\ell_r \mathbf{q}_{\text{LS}}$ of \mathbf{K} corresponding to the maximum positive Eigenvalue of the 4×4 symmetric matrix \mathbf{K} .

From this computed ${}^\ell_r \mathbf{q}_{\text{LS}}$, one can get the rotation matrix ${}^\ell_r \mathbf{R}_{\text{LS}} = \mathcal{R}({}^\ell_r \mathbf{q}_{\text{LS}})$, where the operator $\mathcal{R}(\check{\mathbf{q}} = [q_0, \mathbf{q}^\top]^\top)$ is defined as

$$\mathcal{R}(\check{\mathbf{q}}) \triangleq (q_0^2 - \|\mathbf{q}\|^2) \mathbf{I}_3 + 2\mathbf{q}\mathbf{q}^\top + 2q_0 \mathbf{q} \times \mathbf{I}_3. \quad (18)$$

1) Rotational Covariance Estimation: Judging from the recent literature in the space and aircraft-dynamics community [34], [35], many ways of representing uncertainty in unit quaternions exist. Since the rotation covariance was not estimated as part of points registration [8], [32], we present a new solution, which is based on the Hessian of the cost function [31]. As was the case with the covariance matrix of plane parameters, the covariance ${}^\ell_r \mathbf{C}_{\check{\mathbf{q}}\check{\mathbf{q}}}$ of the unit quaternion ${}^\ell_r \mathbf{q}_{\text{LS}}$ has the feature that the matrix is singular [34], [35] due to the unit-norm constraint. In this paper, we will use this singular 4×4 matrix, which represents the uncertainty of a unit quaternion on the tangent plane of a unit 3-sphere in 4-D.

As there is no uncertainty along the direction of the unit quaternion, ${}^\ell_r \mathbf{C}_{\check{\mathbf{q}}\check{\mathbf{q}}} {}^\ell_r \mathbf{q} = 0$. Such a covariance matrix can be found by computing the Hessian of the constrained Lagrangian $\mathcal{L} \triangleq \zeta_r - \lambda(\check{\mathbf{q}}^\top \check{\mathbf{q}} - 1)$ at $\check{\mathbf{q}} = {}^\ell_r \mathbf{q}_{\text{LS}}$, and $\lambda_{\text{LS}} = \mu_{\max}(\mathbf{K})$, the latter being the maximum Eigenvalue of \mathbf{K} . This Hessian is given by

$$\mathbf{H}_{\check{\mathbf{q}}\check{\mathbf{q}}}({}^\ell_r \mathbf{q}_{\text{LS}}) \triangleq 2(\mathbf{K} - \mu_{\max}(\mathbf{K})\mathbf{I}_4). \quad (19)$$

The unit quaternion ${}^\ell_r \mathbf{q}_{\text{LS}}$ spans the null-space of this Hessian. Finally, the sought covariance is given by

$${}^\ell_r \mathbf{C}_{\check{\mathbf{q}}\check{\mathbf{q}}} = -\mathbf{H}_{\check{\mathbf{q}}\check{\mathbf{q}}}^+({}^\ell_r \mathbf{q}_{\text{LS}}). \quad (20)$$

An alternative method to obtain the covariance is that described in [19], which uses results on perturbation of eigenvectors.

D. Least-Squares Translation After Decoupling

Stacking (4b) for $i = 1, \dots, N$, the translation ${}^\ell_r \mathbf{t}$ should ideally satisfy

$$\begin{aligned} \mathbf{M}_r {}^\ell_r \mathbf{t} &= \mathbf{d} \\ \mathbf{M}_{N \times 3} &\triangleq \begin{bmatrix} {}^\ell \hat{\mathbf{n}}_1^\top \\ \vdots \\ {}^\ell \hat{\mathbf{n}}_N^\top \end{bmatrix}, \mathbf{d}_{N \times 1} \triangleq \begin{bmatrix} {}^\ell d_1 - {}^r d_1 \\ \vdots \\ {}^\ell d_N - {}^r d_N \end{bmatrix}. \end{aligned} \quad (21)$$

Since there is uncertainty in \mathbf{M} as well as in \mathbf{d} , ideally, this should be solved using the method of total LSs (TLS) [36]. However, the standard TLS formulation cannot be used directly because 1) the uncertainty in \mathbf{M} is rowwise correlated and anisotropic, and 2) the matrix \mathbf{M} consists of unit vectors, and therefore, the uncertainty is structured. To our knowledge, the latter problem has not been addressed in the literature in the context of TLS.

Due to its intuitive nature and fast closed-form solution, we will solve (21) with ordinary LSs. This assumes that all of the uncertainty is on the right-hand side, i.e., in \mathbf{d} . A justification for this is provided by (58), which shows that the uncertainties on the two sides of (21) are related.

The diagonal weighting matrix \mathbf{W} is defined as

$$\mathbf{C}_d \triangleq \begin{bmatrix} {}^\ell \mathbf{D}_{1,dd} + {}^r \mathbf{D}_{1,dd} & & \mathbf{0} \\ & \ddots & \\ \mathbf{0} & & {}^\ell \mathbf{D}_{N,dd} + {}^r \mathbf{D}_{N,dd} \end{bmatrix} \quad (22)$$

$$\mathbf{W} \triangleq (\mathbf{C}_d^{-1})^{1/2}. \quad (23)$$

Then, the LS solution minimizes $\|\mathbf{W}(\mathbf{M} \mathbf{t}_r - \mathbf{d})\|$. If \mathbf{M} is full rank, the LSs optimum translation is ${}^\ell_r \mathbf{t}_{\text{LS}} = (\mathbf{M}^\top \mathbf{W}^2 \mathbf{M})^{-1} \mathbf{M}^\top \mathbf{W}^2 \mathbf{d}$.

Unlike rotation, in general, we need $N \geq 3$ mutually nonparallel planes to find ${}^\ell_r \mathbf{t}_{\text{LS}}$. The LSs formula is not a good way to compute the solution because \mathbf{M} may be ill-conditioned, may be rank-deficient, or $N < 3$. A more general way to solve the equation is presented next. We define

$$\hat{\mathbf{M}} \triangleq \mathbf{W} \mathbf{M}, \quad \hat{\mathbf{d}} \triangleq \mathbf{W} \mathbf{d}. \quad (24)$$

Let the singular-value decomposition of $\hat{\mathbf{M}}$ be given by $\mathbf{U}_{N \times N} \mathbf{\Lambda}_{N \times 3} \mathbf{V}_{3 \times 3}^\top$. $\mathbf{\Lambda}$ has nonnegative singular values σ_i^2 arranged in descending order. The column unit vectors of \mathbf{U} are denoted as \mathbf{u}_i , $i = 1, \dots, N$, and the column unit vectors of \mathbf{V} are denoted as \mathbf{v}_i , $i = 1, \dots, 3$.

Let $N_r \leq 3$ be the *effective rank* of $\hat{\mathbf{M}}$. If the largest singular value $\sigma_1^2 < \epsilon_1$, then the effective rank is 0. The parameter ϵ_1 is dependent on machine accuracy. If $\sigma_1^2 \geq \epsilon_1$, then the effective rank is found by finding the count of all singular values

$\sigma_i^2 > \sigma_1^2/\bar{c}$ in the diagonal matrix $\mathbf{\Lambda}$, where \bar{c} is the maximum allowable condition number of the matrix. In practice, ϵ_1 and \bar{c} are quite important parameters to obtain good translation estimates, as well as to identify the directions in which the translation estimate is the most uncertain.

Then, the best rank N_r approximation of $\hat{\mathbf{M}}$ is given by

$$\tilde{\mathbf{M}} = \sum_{i=1}^{N_r} \sigma_i^2 \hat{\mathbf{u}}_i \hat{\mathbf{v}}_i^\top, \quad N_r \leq 3. \quad (25)$$

The span of the orthogonal unit vectors $\hat{\mathbf{u}}_i$, $i = 1, \dots, N_r$ gives the best approximation for the range space of $\hat{\mathbf{M}}$. Therefore, the closest that we can get to $\hat{\mathbf{d}}$ is $\hat{\mathbf{d}} = \sum_{i=1}^{N_r} (\hat{\mathbf{u}}_i \cdot \hat{\mathbf{d}}) \hat{\mathbf{u}}_i$, which gives the corresponding translation estimate

$$\ell_r \mathbf{t}_{LS} = \sum_{i=1}^{N_r} \frac{(\hat{\mathbf{u}}_i \cdot \hat{\mathbf{d}}) \hat{\mathbf{v}}_i}{\sigma_i^2} \triangleq \hat{\mathbf{M}}^+ \hat{\mathbf{d}}, \quad \hat{\mathbf{M}}^+ \triangleq \sum_{i=1}^{N_r} \frac{\hat{\mathbf{v}}_i \hat{\mathbf{u}}_i^\top}{\sigma_i^2}. \quad (26)$$

This is also the minimum 2-norm solution of the LS problem, regardless of the rank of $\hat{\mathbf{M}}$ mentioned in [36].

Note that for directions $\hat{\mathbf{v}}_i$, $i = N_r + 1, \dots, 3$, we have no information about the translation. One option is to keep these components 0 and inject large uncertainty along those directions in the covariance matrix. However, if an estimate by overlap (see Section II-E) or by odometry $\ell_r \mathbf{t}_e$, along with its covariance matrix $\mathbf{C}_{t,e}$ is available, we can use it *only* for these missing components. In this case, we have

$$\begin{aligned} \ell_r \mathbf{t}_{LS} &= \hat{\mathbf{M}}^+ \hat{\mathbf{d}} + \sum_{i=N_r+1}^3 (\ell_r \mathbf{t}_e \cdot \hat{\mathbf{v}}_i) \hat{\mathbf{v}}_i \\ &\triangleq \hat{\mathbf{M}}^+ \hat{\mathbf{d}} + \mathbf{M}_e \ell_r \mathbf{t}_e, \quad \mathbf{M}_e \triangleq \sum_{i=N_r+1}^3 \hat{\mathbf{v}}_i \hat{\mathbf{v}}_i^\top. \end{aligned} \quad (27)$$

Finally, we can write the estimate of the covariance matrix for translation as follows:

$$\begin{aligned} \ell_r \mathbf{C}_{tt} &= \tau \hat{\mathbf{M}}^+ \mathbf{W} \mathbf{C}_d \mathbf{W}^\top (\hat{\mathbf{M}}^+)^T + \mathbf{M}_e \mathbf{C}_{t,e} \mathbf{M}_e^\top \\ &= \tau \mathbf{M}^+ \mathbf{C}_d (\mathbf{M}^+)^T + \mathbf{M}_e \mathbf{C}_{t,e} \mathbf{M}_e^\top \end{aligned} \quad (28)$$

where the last equation comes from simplification using (23) and (24), and

$$\tau \triangleq \frac{1}{N - N_r} \|\hat{\mathbf{M}} \ell_r \mathbf{t}_{LS} - \hat{\mathbf{d}}\|^2. \quad (29)$$

In this study, we have used the overlap estimate, which is described in Section II-E, to supply the translation along missing $3 - N_r$ directions instead of the odometry, since, in general, overlap estimates tend to be much more accurate than odometry.

E. Roughly Estimating Translation by Overlap

Section II-D provided an accurate method to determine translation when planar patches with normals in all directions are present. When, however, corresponding planes normal to certain directions are missing, we need to estimate the translation along these directions using other methods, which are less accurate. In this section, we consider one such method, which is based on the assumption of complete overlap of planes. In general,

this will only be accurate if there are no occlusions present, and sensor sampling is uniform. Additionally, this method requires that a rotation estimate of $\ell_r \mathbf{R}$ be known.

Fortunately, as shown in Appendix A, all the required information for using overlap is already present in the 4×4 plane-parameter covariance matrix $\mathbf{C} = -\mathbf{H}^+$. Letting \mathbf{H}_{dd} denote the last diagonal element of \mathbf{H} , the weighted center of mass \mathbf{p}_c of the patch can be computed by (50b), and the scatter of the points *on the patch plane* (not normal to it) is given by $(-1/\mathbf{H}_{dd})(\mathbf{D}_{\hat{\mathbf{n}}\hat{\mathbf{n}}})^+$. This can be seen by using (50) and (49) in the definition (61), which gives

$$\begin{aligned} (-1/\mathbf{H}_{dd})(\mathbf{D}_{\hat{\mathbf{n}}\hat{\mathbf{n}}})^+ &= \frac{1}{\sum_j w_j} \sum_j w_j (\mathbf{p}_j - \mathbf{p}_c)(\mathbf{p}_j - \mathbf{p}_c)^\top \\ &\quad - \frac{1}{\sum_j w_j} \sum_j w_j \hat{\mathbf{n}}^\top (\mathbf{p}_j - \mathbf{p}_c)(\mathbf{p}_j - \mathbf{p}_c)^\top \hat{\mathbf{n}} \mathbf{I} \end{aligned} \quad (30)$$

where the summation is on all points belonging to the planar patch with normal $\hat{\mathbf{n}}$. To this, we can add the uncertainty along the direction of the normal and define the total overlap uncertainty as

$$\mathbf{C}_{pp} \triangleq (-1/\mathbf{H}_{dd})(\mathbf{D}_{\hat{\mathbf{n}}\hat{\mathbf{n}}})^+ + \mathbf{D}_{dd}(\hat{\mathbf{n}}\hat{\mathbf{n}}^\top). \quad (31)$$

Note that we take the scatter to be a conservative measure of uncertainty because the whole patch may not be visible in the sample owing to occlusion. This is usually the case in practice.

Suppose, we are given a set of pairs of corresponding planes, with point-cloud centers back-computed by (50b) as $\ell_r \mathbf{p}_{c,i}$, $r \mathbf{p}_{c,i}$, $i = 1, \dots, N$, and suppose further that the rotation $\ell_r \mathbf{R}$ is known beforehand. The translation and its covariance for the i th pair can then be estimated as

$$\ell_r \mathbf{t}_i \approx \ell_r \mathbf{p}_{c,i} - \ell_r \mathbf{R} r \mathbf{p}_{c,i} \quad (32)$$

$$\ell_r \mathbf{C}_{t,i} \approx \ell_r \mathbf{C}_{pp,i} + \ell_r \mathbf{R} r \mathbf{C}_{pp,i} \ell_r \mathbf{R}^\top. \quad (33)$$

The bigger the plane patch, the higher is the variance in the translation estimate found using it. We have N such estimates. We can then estimate the translation from overlap as

$$\ell_r \mathbf{t}_e = \arg \min_{\mathbf{t}} \chi_e^2(\mathbf{t}),$$

$$\chi_e^2(\mathbf{t}) \triangleq \frac{1}{2} \sum_i^N (\ell_r \mathbf{t}_i - \mathbf{t})^\top (\ell_r \mathbf{C}_{t,i})^{-1} (\ell_r \mathbf{t}_i - \mathbf{t}). \quad (34)$$

The standard closed-form solution for this is given by

$$\mathbf{A} \triangleq \sum_{i=1}^N (\ell_r \mathbf{C}_{t,i})^{-1}, \quad \mathbf{b} \triangleq \sum_{i=1}^N (\ell_r \mathbf{C}_{t,i})^{-1} \ell_r \mathbf{t}_i. \quad (35)$$

$$\ell_r \mathbf{t}_e = \mathbf{A}^{-1} \mathbf{b}. \quad (36)$$

The optimistic covariance of this estimate is given by

$$\mathbf{C}_{t,e} = \frac{\kappa \chi_e^2(\ell_r \mathbf{t}_e)}{3N - 3} \left(\sum_{i=1}^N (\ell_r \mathbf{C}_{t,i})^{-1} \right)^{-1} \quad (37)$$

where $\kappa > 1$ accounts for the presence of occlusions in the scene.

III. ASSIGNING UNKNOWN CORRESPONDENCES

Up until now, we have assumed that the correspondences between the planes in the two successive views are known. Now, we drop this assumption and explore ways of answering “which plane is which?” If the i th plane in the left frame corresponds to the j th one in the right, then it will be denoted as ${}^\ell\mathcal{P}_i \leftrightarrow {}^r\mathcal{P}_j$, which is abbreviated $i \leftrightarrow j$. We first consider some simple tests that help us to decide whether $i \leftrightarrow j$ is potentially true. This will help prune the search space of possible correspondences. Out of this reduced search space, we shall later extract the correspondences that give the minimum uncertainty volume of registration.

A. Some Tests for Pruning the Correspondence Search Space

1) *Size-Similarity Test*: As shown in Appendix A, the inverse of the 4×4 covariance matrix of the plane parameters is proportional to the number of points in the plane. Therefore, the determinant of this matrix is proportional to the fourth power of the size of the point cloud, and it is also a function of the associated certainty of the points. One way to restrict the correspondence search space is to discard pairs for which the log of the ratio of this value exceeds some threshold, i.e., we discard the possibility that $i \leftrightarrow j$ if

$$|\log |{}^\ell\mathbf{C}_i^+|_+ - \log |{}^r\mathbf{C}_j^+|_+| > \bar{L}_{\text{det}}. \quad (38)$$

2) *Given Translation-Agreement Test*: If an estimate of the translation ${}^\ell\mathbf{t}_e$ is given along with its covariance \mathbf{C}_{tt} and a potential correspondence ${}^\ell\mathcal{P}_i \leftrightarrow {}^r\mathcal{P}_j$, (4b) can be used again to form an error metric given by

$$\chi_{t,e}^2 \triangleq \frac{({}^\ell\hat{\mathbf{n}}_i \cdot {}^\ell\mathbf{t}_e - {}^\ell d_i + {}^r d_j)^2}{{}^\ell\mathbf{D}_{i,dd} + {}^r\mathbf{D}_{j,dd} + {}^\ell\mathbf{t}_e^\top {}^\ell\mathbf{D}_{i,\hat{\mathbf{n}}\hat{\mathbf{n}}} {}^\ell\mathbf{t}_e + {}^\ell\hat{\mathbf{n}}_i^\top \mathbf{C}_{\text{tt}} {}^\ell\hat{\mathbf{n}}_i}. \quad (39)$$

If $\chi_{t,e}^2 > \bar{\chi}_t^2$, the hypothesis that the potential correspondence agrees with the given translation is rejected.

3) *Odometry Rotation-Agreement Test*: Similarly, if the roll (ψ_o), pitch (θ_o), and yaw (ϕ_o) angles for ${}^\ell\mathbf{R}$, according to odometry, are given along with their covariance matrix $\mathbf{C}_{\phi,\theta,\psi}$, we can use them to eliminate potential correspondence pairings that cause a gross disagreement with the odometry values. Suppose we have selected two pairs of corresponding normals ${}^\ell\hat{\mathbf{n}}_i, {}^r\hat{\mathbf{n}}_i, i = 1, 2$. If these pairs are nonparallel, the rotation is fully determined and can be computed as ${}^\ell\mathbf{R}$ from the results of Section II-C. From ${}^\ell\mathbf{R}$, the corresponding roll (ψ), pitch (θ), and yaw (ϕ) angles can be extracted. Then, the Mahalanobis distance is computed as

$$\mathbf{e}_r \triangleq \begin{bmatrix} \phi_o - \phi \\ \theta_o - \theta \\ \psi_o - \psi \end{bmatrix}, \chi_{R,o}^2 \triangleq \mathbf{e}_r^\top \mathbf{C}_{\phi,\theta,\psi}^{-1} \mathbf{e}_r. \quad (40)$$

If $\chi_{R,o}^2 > \bar{\chi}_{R,o}^2$, we can reject the hypothesis that the selected correspondences agree with the odometry.

In this paper, we use odometry only as a switch to restrict the search space for correspondences. Within this space, however, there is no *attraction* toward the odometry estimation. Thus, even if actual odometry is unavailable, but some reasonable bounds for pose change are known, they can still be used.

4) *Plane-Patch Overlap Test*: In certain rare cases, there might be more than one patch with very close $(\hat{\mathbf{n}}, d)$ values—imagine two picture frames on the same wall. Disambiguating among them is usually not necessary for relative-pose estimation, if there are planes perpendicular to these patches. If, however, no such plane is found, then there is uncertainty about the translation parallel to the infinite plane containing the two patches. In such a case, the only way to disambiguate the patch-correspondences across two views is to consider whether one planar patch overlaps with another after application of rotation and translation. If we calculate such estimates for two pairs of supposedly corresponding planes i, j , then we can compute an overlap-translation estimate for each of the pairs using the method described in Section II-E. Two such estimates will be considered consistent if

$$\mathbf{e}_{ij} \triangleq {}^\ell\mathbf{t}_i - {}^\ell\mathbf{t}_j, \bar{\chi}_{\text{ovlp}}^2 \geq \mathbf{e}_{ij}^\top ({}^\ell\mathbf{C}_{i,t} + {}^\ell\mathbf{C}_{j,t})^{-1} \mathbf{e}_{ij}. \quad (41)$$

5) *Cross-Angle Test*: In a rigid motion, the angles between normals in one sample should be the same as the corresponding angles in the next. Suppose we are given planes normals and covariances $\{{}^\ell\hat{\mathbf{n}}_{i_1}, {}^\ell\mathbf{D}_{i_1,\hat{\mathbf{n}}\hat{\mathbf{n}}}\}, \{{}^\ell\hat{\mathbf{n}}_{j_1}, {}^\ell\mathbf{D}_{j_1,\hat{\mathbf{n}}\hat{\mathbf{n}}}\}$ in the left scene and $\{{}^r\hat{\mathbf{n}}_{i_2}, {}^r\mathbf{D}_{i_2,\hat{\mathbf{n}}\hat{\mathbf{n}}}\}, \{{}^r\hat{\mathbf{n}}_{j_2}, {}^r\mathbf{D}_{j_2,\hat{\mathbf{n}}\hat{\mathbf{n}}}\}$ in the right scene, such that potentially, ${}^\ell\hat{\mathbf{n}}_{i_1} \leftrightarrow {}^r\hat{\mathbf{n}}_{i_2}$ and ${}^\ell\hat{\mathbf{n}}_{j_1} \leftrightarrow {}^r\hat{\mathbf{n}}_{j_2}$. Ideally

$${}^\ell v_{i_1,j_1} \triangleq {}^\ell\hat{\mathbf{n}}_{j_1}^\top {}^\ell\hat{\mathbf{n}}_{i_1}, {}^r v_{i_2,j_2} \triangleq {}^r\hat{\mathbf{n}}_{j_2}^\top {}^r\hat{\mathbf{n}}_{i_2}, {}^\ell v_{i_1,j_1} \approx {}^r v_{i_2,j_2}. \quad (42)$$

The variance of ${}^\ell v_{i_1,j_1}$ is ${}^\ell\sigma_{i_1,j_1}^2 \approx {}^\ell\hat{\mathbf{n}}_{j_1}^\top {}^\ell\mathbf{D}_{i_1,\hat{\mathbf{n}}\hat{\mathbf{n}}} {}^\ell\hat{\mathbf{n}}_{j_1} + {}^\ell\hat{\mathbf{n}}_{i_1}^\top {}^\ell\mathbf{D}_{j_1,\hat{\mathbf{n}}\hat{\mathbf{n}}} {}^\ell\hat{\mathbf{n}}_{i_1}$ and ${}^r\sigma_{i_2,j_2}^2$ is similarly defined. A distance metric can be defined as

$$\chi_x^2 \triangleq \frac{({}^\ell v_{i_1,j_1} - {}^r v_{i_2,j_2})^2}{{}^\ell\sigma_{i_1,j_1}^2 + {}^r\sigma_{i_2,j_2}^2}. \quad (43)$$

If $\chi_x^2 > \bar{\chi}_x^2$, we can reject the assumed correspondences. This is our main test for geometric consistency.

6) *Parallel Consistency Test*: Given two potentially corresponding pairs ${}^\ell\mathcal{P}_{i_1} \leftrightarrow {}^r\mathcal{P}_{i_2}$ and ${}^\ell\mathcal{P}_{j_1} \leftrightarrow {}^r\mathcal{P}_{j_2}$, such that either both ${}^\ell\hat{\mathbf{n}}_{i_1} \cdot {}^\ell\hat{\mathbf{n}}_{j_1} \approx 1$ and ${}^r\hat{\mathbf{n}}_{i_2} \cdot {}^r\hat{\mathbf{n}}_{j_2} \approx 1$, or both ${}^\ell\hat{\mathbf{n}}_{i_1} \cdot {}^\ell\hat{\mathbf{n}}_{j_1} \approx -1$ and ${}^r\hat{\mathbf{n}}_{i_2} \cdot {}^r\hat{\mathbf{n}}_{j_2} \approx -1$, i.e., the planes are parallel or antiparallel. Then, on using (4b), we should also have $\delta \triangleq ({}^\ell d_{i_1} - {}^r d_{i_2}) \mp ({}^\ell d_{j_1} - {}^r d_{j_2}) \approx 0$, where the $+$ is taken for the antiparallel case. This can be checked by computing

$$\chi_\delta^2 \triangleq \frac{\delta^2}{{}^\ell\mathbf{D}_{i_1,dd} + {}^\ell\mathbf{D}_{j_1,dd} + {}^r\mathbf{D}_{i_2,dd} + {}^r\mathbf{D}_{j_2,dd}}. \quad (44)$$

The consistency hypothesis can be rejected if the $\chi_\delta^2 > \bar{\chi}_\delta^2$.

B. Minimally Uncertain Maximal-Consensus Algorithm

Given an average of N planes per view, there are $(N+1)!$ possible correspondences, if we include the case when a plane in one view is not present in the other. We can naively try all of these correspondences, possibly using the extra tests

of Section III-A to cut down the search space, and choose the one with the maximum overall consistency. Typically, the number of planes is much less than the number of points used to compute them. Therefore, such an exhaustive search may work for a small value of N . Next, we present a novel algorithm, which aims to find the most consistent set with respect to rotation and translation. It uses the fact that to uniquely determine rotation, one needs to know at least two nonparallel-plane correspondence pairs and, for translation, at least three. Nonparallel-planes' correspondences have rotation information, and parallel-planes' correspondences have only translation information.

The algorithm initially finds all consistent two pairs of correspondences (i.e., quadruplets) in its preprocessing step using the tests devised in the last sections. In the main search step, each of these pairs are considered in turn, and their largest rotation and translation consensus sets are built. For each of these consensus sets, the LSs rotation and translation are determined, along with the volume of uncertainty given by the pseudodeterminant of the covariance matrix of the pose registration. The consensus set of a certain minimum size N_C (which is explained later), which has the minimum value of the uncertainty volume, is selected as the chosen set of correspondences.

Although a formulation of RANSAC for plane-matching itself would have been novel enough since its robustly proven application in this field is currently lacking in the literature, we have added further improvements to the procedure. Unlike RANSAC, there is no random search, and instead of a greedy maximum consensus, a minimum-uncertainty-volume approach is taken. We have found this approach to be much more stable, in practice, than one based solely on the size of the consensus set. The uncertainty volume automatically decreases if more *consistent* correspondence pairs are added to the set. If, however, a pair is added, which merely passes the consistency thresholds, but is not overall consistent, the uncertainty volume increases. This also removes the necessity of over-tuning the thresholds in the consistency tests.

Before we go on to the algorithm, the basic notations used in this section are summarized as follows.

$\#\Omega$	size of the set or list Ω ;
$\omega \cdot a$	member a of a tuple ω ;
${}^\ell \mathcal{P}_i \parallel {}^\ell \mathcal{P}_j$	planes i and j in the ℓ set are parallel;
${}^r \mathcal{P}_i \parallel {}^r \mathcal{P}_j$	planes i and j in the r set are antiparallel;
${}^\ell \mathcal{P}_i \nparallel {}^\ell \mathcal{P}_j$	planes are neither parallel nor antiparallel;
${}^\ell \mathcal{P}_i \leftrightarrow {}^r \mathcal{P}_j$	${}^\ell \mathcal{P}_i$ and ${}^r \mathcal{P}_j$ correspond to each other.

A test for parallelism can be devised by testing for nearness of the dot product to unity within some threshold or a statistical measure can be derived along the lines of (43).

We consider the following consistency requirements in increasing order of complexity.

- 1) A potential correspondence ${}^\ell \mathcal{P}_i \leftrightarrow {}^r \mathcal{P}_j$ is called *1-consistent* if it passes the size-similarity test (38) and the translation-agreement test (see Section III-A2) for odometry, if available.
- 2) Two potential correspondences ${}^\ell \mathcal{P}_{i_1} \leftrightarrow {}^r \mathcal{P}_{i_2}$ and ${}^\ell \mathcal{P}_{j_1} \leftrightarrow {}^r \mathcal{P}_{j_2}$ are termed as the following.

Algorithm 1: MUMC Preprocessing Step: Find all consistent correspondence pairs

input : Left planes indexed list
 ${}^\ell \mathcal{P} = \{\langle {}^\ell \hat{\mathbf{n}}_i, {}^\ell d_i, {}^\ell \mathbf{C}_i \rangle \mid i = 1 \dots N_\ell\}$, and right
planes indexed list
 ${}^r \mathcal{P} = \{\langle {}^r \hat{\mathbf{n}}_i, {}^r d_i, {}^r \mathbf{C}_i \rangle \mid i = 1 \dots N_r\}$.

output: Sets $\Omega_\parallel, \Omega_\nparallel$.

- 1 Sort planes in descending order of evidence, i.e., $|{}^s \mathbf{C}_i^+|_+$, $s = r/\ell$ and take a certain top $F_t\%$.
- 2 Compute decoupled covariances using the procedure in Sec. II-B. Make a list \mathcal{L} of all unique and *1-consistent* potentially corresponding pairs $({}^\ell \mathcal{P}_i \leftrightarrow {}^r \mathcal{P}_j)$, $i = 1 \dots N_\ell$, $j = 1 \dots N_r$. Obviously, $\#\mathcal{L} \leq N_\ell \times N_r$.
- 3 **for** $k = 1 \dots \#\mathcal{L} - 1$ **do**
- 4 $({}^\ell \mathcal{P}_{k_1} \leftrightarrow {}^r \mathcal{P}_{k_2}) \leftarrow \mathcal{L}[k]$
- 5 **for** $i = k + 1 \dots \#\mathcal{L}$ **do**
- 6 $({}^\ell \mathcal{P}_{i_1} \leftrightarrow {}^r \mathcal{P}_{i_2}) \leftarrow \mathcal{L}[i]$
- 7 **if** $\mathcal{L}[k], \mathcal{L}[i]$ *translation 2-consistent* **then**
- 8 Compute χ_δ^2 from parallel consistency test (44)
- 9 If the above test passed, add $\langle {}^\ell \mathcal{P}_{k_1} \leftrightarrow {}^r \mathcal{P}_{k_2}, {}^\ell \mathcal{P}_{i_1} \leftrightarrow {}^r \mathcal{P}_{i_2}, \chi_\delta^2 \rangle$ to Ω_\parallel
- 10 **else if** $\mathcal{L}[k], \mathcal{L}[i]$ *rotation 2-consistent* **then**
- 11 Compute χ_\times^2 from cross-angle consistency test (43)
- 12 If the above test passed, add $\langle {}^\ell \mathcal{P}_{k_1} \leftrightarrow {}^r \mathcal{P}_{k_2}, {}^\ell \mathcal{P}_{i_1} \leftrightarrow {}^r \mathcal{P}_{i_2}, \chi_\times^2 \rangle$ to Ω_\nparallel
- 13 **end**
- 14 **end**
- 15 **end**

- a) *Rotation-2-consistent:* If ${}^\ell \mathcal{P}_{i_1} \nparallel {}^\ell \mathcal{P}_{j_1}$ and ${}^r \mathcal{P}_{i_2} \nparallel {}^r \mathcal{P}_{j_2}$, then a unique 3-D rotation estimate ${}^\ell \mathbf{R}$ can be computed from the assumption that ${}^\ell \mathcal{P}_{i_1} \leftrightarrow {}^r \mathcal{P}_{i_2}$ and ${}^\ell \mathcal{P}_{j_1} \leftrightarrow {}^r \mathcal{P}_{j_2}$. If they pass the cross-angle test (see Section III-A5), the overlap test of Section III-A4, and the test of (40), if odometry is available, then the pair is rotation-2-consistent.
- b) *Translation-2-consistent:* If either ${}^\ell \mathcal{P}_{i_1} \parallel {}^\ell \mathcal{P}_{j_1}$ and ${}^r \mathcal{P}_{i_2} \parallel {}^r \mathcal{P}_{j_2}$, or ${}^\ell \mathcal{P}_{i_1} \parallel {}^\ell \mathcal{P}_{j_1}$ and ${}^r \mathcal{P}_{i_2} \nparallel {}^r \mathcal{P}_{j_2}$, then in addition, the two pairs pass the parallel consistency test of Section III-A6.

The first step of the algorithm, which is shown in Algorithm 1, consists of collecting all nonparallel rotationally 2-consistent correspondence pairs in set Ω_\nparallel and all parallel and translationally 2-consistent pairs in set Ω_\parallel . Both sets consist of elements, which are tuples of format $\langle \{ {}^\ell \mathcal{P}_{i_1} \leftrightarrow {}^r \mathcal{P}_{i_2}, {}^\ell \mathcal{P}_{j_1} \leftrightarrow {}^r \mathcal{P}_{j_2} \}, \chi^2 \rangle$. For notational convenience and due to symmetry, the *order* of the two pairs in the tuple is not important. Hence, the aforementioned tuple is the same as the tuple $\langle \{ {}^\ell \mathcal{P}_{j_1} \leftrightarrow {}^r \mathcal{P}_{j_2}, {}^\ell \mathcal{P}_{i_1} \leftrightarrow {}^r \mathcal{P}_{i_2} \}, \chi^2 \rangle$. We can define the following.

Algorithm 2: MUMC Main Search: Finding minimally uncertain maximal consensus

input : Ω_{\parallel} and $\Omega_{\#}$ from the output of Algo. 1.

output: The resolved correspondences and the computed transform.

```

1 Set Minimum required consensus size  $N_C \leftarrow 4$ .
2 Initialize the potential solution list  $\mathcal{W} \leftarrow \emptyset$ .
3 Initialize selected solution tuple  $\bar{\omega} \leftarrow \emptyset$ .
4 for  $\forall \ell \mathcal{P}_{i_1} \leftrightarrow r \mathcal{P}_{i_2} \in \mathcal{K}$  do
5   Find the maximal rotation consensus set  $\Gamma_{\#}$  in
      $[\ell \mathcal{P}_{i_1} \leftrightarrow r \mathcal{P}_{i_2}]_{\#}$ .
6   Find the maximal parallel consensus set  $\Gamma_{\parallel}$  in
      $[\ell \mathcal{P}_{i_1} \leftrightarrow r \mathcal{P}_{i_2}]_{\parallel}$ .
7   Find the maximal set  $\Gamma_t$  in  $\Gamma_{\#}$  which is
     translationally consistent.
8   Append  $\Gamma \leftarrow \Gamma_t \cup \Gamma_{\parallel}$ .
9   Using  $\Gamma$ , and results of Sec. II, compute the rotation
      $\ell \hat{\mathbf{R}}$  and its covariance  $\ell \mathbf{C}_{\hat{\mathbf{R}}}$ , and translation  $\ell \mathbf{t}$  and
     its covariance  $\ell \mathbf{C}_{\mathbf{t}}$ .
10  Compute uncertainty-volume metric
      $\alpha = |\ell \mathbf{C}_{\mathbf{t}}| \times |\ell \mathbf{C}_{\hat{\mathbf{R}}}|$ .
11  Assign tuple  $\omega_i \leftarrow \langle \alpha, \Gamma, \ell \hat{\mathbf{R}}, \ell \mathbf{t}, \ell \mathbf{C}_{\hat{\mathbf{R}}}, \ell \mathbf{C}_{\mathbf{t}} \rangle$  and
     append to  $\mathcal{W}$ .
12  if  $\#(\omega_i, \Gamma) \geq N_C$  or  $\#(\bar{\omega}, \Gamma) \leq N_C$  then
13    if  $\omega_i, \alpha < \bar{\omega}, \alpha$  then
14       $\bar{\omega} \leftarrow \omega_i$ 
15    end
16  end
17 end
18 The tuple  $\bar{\omega}$  is the chosen solution. Other potential
    solutions are in the list  $\mathcal{W}$ .

```

- 1) A set of interesting pairs \mathcal{K} , such that the correspondence $\ell \mathcal{P}_{i_1} \leftrightarrow r \mathcal{P}_{i_2} \in \mathcal{K}$ if it exists in any of the tuples in Ω_{\parallel} or $\Omega_{\#}$.
- 2) A set of correspondences, which are translation-2-consistent to a given correspondence

$$[\ell \mathcal{P}_{i_1} \leftrightarrow r \mathcal{P}_{i_2}]_{\parallel} \triangleq \left\{ \langle \ell \mathcal{P}_{j_1} \leftrightarrow r \mathcal{P}_{j_2}, \chi^2 \rangle \mid \langle \ell \mathcal{P}_{j_1} \leftrightarrow r \mathcal{P}_{j_2}, \ell \mathcal{P}_{i_1} \leftrightarrow r \mathcal{P}_{i_2} \rangle \in \Omega_{\parallel} \right\}. \quad (45)$$

The reader is reminded of the order irrelevance within a tuple due to symmetry.

- 3) A set of correspondences, which are not parallel or antiparallel to a given correspondence, but are *rotation-2-consistent* with it

$$[\ell \mathcal{P}_{i_1} \leftrightarrow r \mathcal{P}_{i_2}]_{\#} \triangleq \left\{ \langle \ell \mathcal{P}_{j_1} \leftrightarrow r \mathcal{P}_{j_2}, \chi^2 \rangle \mid \langle \ell \mathcal{P}_{j_1} \leftrightarrow r \mathcal{P}_{j_2}, \ell \mathcal{P}_{i_1} \leftrightarrow r \mathcal{P}_{i_2} \rangle \in \Omega_{\#} \right\}. \quad (46)$$

The second step, which is shown in Algorithm 2, considers each member of \mathcal{K} and finds the member with the minimum uncertainty in the determination of $\ell \mathbf{t}$ and $\ell \mathbf{R}$. We first give an overview skeleton of the algorithm in Algorithm 2. Lines 1, 5, 6, 7, and 9 are explained afterward.

Explanation of Line 1: N_C is set to 4, because the minimum number of corresponding pairs required to uniquely compute translation is 3. Therefore, we can speak of “consensus” only if we have ≥ 4 pairs in agreement.

Explanation of Line 5: We first note that a rotation $\ell \mathbf{R}$ can be uniquely found by freezing the correspondences $\ell \mathcal{P}_{i_1} \leftrightarrow r \mathcal{P}_{i_2}$, and another one $\langle \ell \mathcal{P}_{j_1} \leftrightarrow r \mathcal{P}_{j_2}, \chi^2 \rangle \in [\ell \mathcal{P}_{i_1} \leftrightarrow r \mathcal{P}_{i_2}]_{\#}$. A third correspondence $\langle \ell \mathcal{P}_{k_1} \leftrightarrow r \mathcal{P}_{k_2}, \chi^2 \rangle \in [\ell \mathcal{P}_{i_1} \leftrightarrow r \mathcal{P}_{i_2}]_{\#}$ is called rotationally consistent with the two frozen correspondences, if $\ell \hat{\mathbf{n}}_{k_1} \cdot (\ell \mathbf{R}^T \hat{\mathbf{n}}_{k_2}) \approx 1$. A test analogous to (43), or even a threshold-based test, can be used here. We have used a lower threshold of 0.9980 for all sensors. The set of all rotationally consistent correspondences to the frozen pair is denoted $\Omega_R(\ell \mathcal{P}_{i_1} \leftrightarrow r \mathcal{P}_{i_2}, \ell \mathcal{P}_{j_1} \leftrightarrow r \mathcal{P}_{j_2})$, and its overall $\sum \chi^2_{\times}$ can be evaluated by summing up the χ^2_{\times} values of all tuples belonging to the set. We then find the largest such set, which is denoted by $\Omega_R^*(\ell \mathcal{P}_{i_1} \leftrightarrow r \mathcal{P}_{i_2})$, by considering all $\ell \mathcal{P}_{j_1} \leftrightarrow r \mathcal{P}_{j_2}$, where, if two sets are of equal size, then the one having lower overall $\sum \chi^2_{\times}$ is taken. The set $\Omega_R^*(\ell \mathcal{P}_{i_1} \leftrightarrow r \mathcal{P}_{i_2})$ may still contain nonunique correspondences, i.e., some plane in the ℓ set may be mapped to more than one other planes in the r set and *vice versa*. The uniqueness problem is solved by sorting all $\langle \ell \mathcal{P}_{k_1} \leftrightarrow r \mathcal{P}_{k_2}, \chi^2 \rangle \in \Omega_R^*(\ell \mathcal{P}_{i_1} \leftrightarrow r \mathcal{P}_{i_2})$ in increasing order of χ^2_{\times} and then fixing correspondences by traversing the sorted list. If $\ell \mathcal{P}_{k_1}$ can be matched with more than one plane in the r set, then the pairing with the lower χ^2_{\times} is automatically chosen. Similar reasoning applies if $r \mathcal{P}_{k_2}$ can be matched with more than one plane in the ℓ set. The reduced and consistent unique set of correspondences is the maximal rotation consensus set $\Gamma_{\#}$.

Explanation of Line 6: The set $[\ell \mathcal{P}_{i_1} \leftrightarrow r \mathcal{P}_{i_2}]_{\parallel}$ may also contain nonunique correspondences, i.e., some plane in the ℓ set may be mapped to more than one of the other planes in the r set and *vice versa*. The uniqueness problem is solved by sorting all $\langle \ell \mathcal{P}_{k_1} \leftrightarrow r \mathcal{P}_{k_2}, \chi^2_{\delta} \rangle \in [\ell \mathcal{P}_{i_1} \leftrightarrow r \mathcal{P}_{i_2}]_{\parallel}$ in increasing order of χ^2_{δ} and then fixing correspondences by traversing the sorted list. If $\ell \mathcal{P}_{k_1}$ can be matched with more than one plane in the r set, then the pairing with the lower χ^2_{δ} is automatically chosen. Similar reasoning applies if $r \mathcal{P}_{k_2}$ can be matched with more than one plane in the ℓ set. The reduced and consistent unique set of correspondences is the maximal parallel consensus set Γ_{\parallel} .

Explanation of Line 7: Here, we find the largest subset of $\Gamma_{\#}$, which is translationally consistent. Unlike rotation, here, we need to freeze three correspondences to compute translation. The first $\ell \mathcal{P}_{i_1} \leftrightarrow r \mathcal{P}_{i_2}$ is given; we take two others $\ell \mathcal{P}_{j_1} \leftrightarrow r \mathcal{P}_{j_2}, \ell \mathcal{P}_{k_1} \leftrightarrow r \mathcal{P}_{k_2} \in \Gamma_{\#}$. Using these, we can compute $\ell \mathbf{t}$. We then find all correspondences $\ell \mathcal{P}_{p_1} \leftrightarrow r \mathcal{P}_{p_2} \in \Gamma_{\#}$, which pass the given translation-agreement test of Section III-A2 for $\ell \mathbf{t}$. For each such test evaluation, we also get a $\chi^2_{t,e}$ value. We denote the set of all such translationally consistent correspondences as $\Omega_t(\ell \mathcal{P}_{i_1} \leftrightarrow r \mathcal{P}_{i_2}, \ell \mathcal{P}_{j_1} \leftrightarrow r \mathcal{P}_{j_2}, \ell \mathcal{P}_{k_1} \leftrightarrow r \mathcal{P}_{k_2})$. This set is also associated with an overall $\sum \chi^2_{t,e}$ value, which is the sum of $\chi^2_{t,e}$ for all the correspondences in it. The maximal such set for all $\ell \mathcal{P}_{j_1} \leftrightarrow r \mathcal{P}_{j_2}$ and $\ell \mathcal{P}_{k_1} \leftrightarrow r \mathcal{P}_{k_2}$ is termed Γ_t , where, if

TABLE I
SENSOR CHARACTERISTICS

	Swiss-ranger	USF Odetics	ALRF
FOV $h \times v$	$47^\circ \times 39^\circ$	$60^\circ \times 60^\circ$	$270^\circ \times 180^\circ$
Resolution $h \times v$	176×144	128×128	541×361
Total points	25,344	16,384	195,301
Range (mm)	7,500	unknown	$> 16,000$

TABLE II
MUMC PARAMETERS (UNITS IN MILLIMETERS AND RADIAN) (S.D. STANDS FOR SCENE-DEPENDENT)

Parameter	Swiss-ranger	USF Odetics	ALRF
$F_t\%$	≥ 50	≥ 80	15 – S.D.
ϵ_1, \bar{c}	$10^{-7}, 25 - 50$	$10^{-7}, 5 - 10$	$10^{-7}, 50 - 70$
L_{det}	4 – 20	10 – 20	10 – 20
$\bar{\chi}_{\text{ovlp}}^2$	2.5 – 4	2.5 – 4	2 – 4
$\bar{\chi}_{\times}^2$	$(1 - 100) \times 10^5$	$(1 - 100) \times 10^5$	$(3 - 10) \times 10^5$
$\bar{\chi}_{\parallel}^2$	10 – 300	200 – 300	10 – 200
$\chi_{t,e}^2$	$\chi_{1,1.5\%}^2 = 3.84$	$\chi_{1,1.5\%}^2$	$\chi_{1,1.5\%}^2$
κ	6	6	6

two sets are of equal size, then the one with the overall lesser value of $\sum \chi_{t,e}^2$ is preferred.

Explanation of Line 9: This line shows that we reuse the results of LSs registration estimation for known correspondences from Section II, including the associated rotation and translation covariances, to evaluate the goodness of the assumed correspondence set Γ .

IV. RESULTS

We present results for three sensors: 1) SR, 2) University of South Florida (USF) Odetics, and 3) a SICK S300 LRF, actuated (pitched) using a servo (ALRF). The characteristics of these sensors are listed in Table I, which shows that the first two are small field-of-view (FOV) sensors and that ALRF has a large FOV. The computation times, which are mentioned in this paper, are for an AMD Turion 2 \times 64, 1.6-GHz laptop with 960-MB RAM running OpenSUSE 10.3 O/S.

A. Selection of Parameters

For parameter and threshold values used by us for various sensors, see Table II. For most parameters, we have provided an approximate range of values that work. In most cases, the ranges for different sensors for a given parameter overlap. When a simple chi-square test from standard tables suffices, only a single value is given. For example, in the last row, $\chi_{1,1.5\%}^2$ means the χ^2 -value for 1 degree of freedom (DOF) at a significance level of 1.5% [30].

Obviously, these parameters depend on the error model considered for the sensor while extracting the planes. For each sensor, a parameter tuning is required once. The observed values of some manually registered planes can be used to arrive at these thresholds. Lower values of thresholds are better because they provide more initial filtering and, thus, speed up the algorithm.

The size-similarity threshold \bar{L}_{det} and overlap threshold $\bar{\chi}_{\text{ovlp}}^2$ also depend on the amount of occlusion present in the scene and the rotational and translational distance at which the samples are taken. They need to be reduced when the occlusion is severe

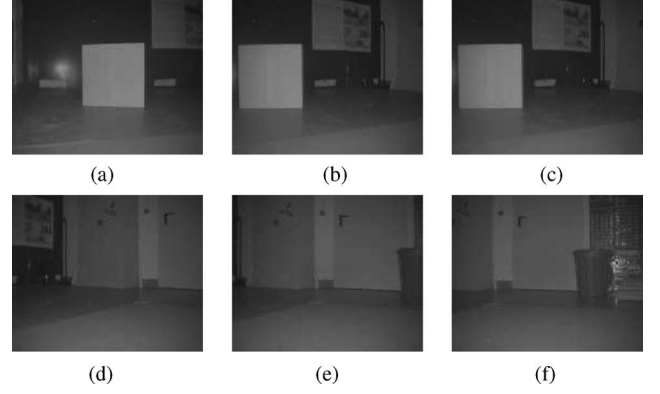


Fig. 2. Intensity images obtained from the SR. The planes were extracted from the corresponding range images. The MUMC result is shown in Fig. 3.

TABLE III
COMPUTATION TIMES (IN SECONDS) FOR PREPROCESSING STEP FOR SR

Scan Nr.	Region Growing	Nr. Patches	Polygonization
1	0.52	39	0.38
2	0.38	25	0.35
3	0.38	25	0.34
4	0.4	13	0.41
5	0.39	15	0.42
6	0.51	23	0.52

or the odometry is not available; otherwise, false matches may result. The filtering F_t is selected so that for low-FOV sensors, most of the planes are retained, while for high-FOV sensors, many low-evidence planes can be filtered out to pick up speed.

B. Swiss-Ranger Rotation Dataset

A test sequence of overlapping views, which is taken from an onboard SR, is shown in Fig. 2. This dataset is particularly interesting because of the relatively large rotation of the robot between every pair of successive views. The computation times for planar-patch extraction using region-growing and for polygonization is shown in Table III.

The results of scan matching using the MUMC algorithm are shown in Fig. 3(c) and (d). We emphasize that no odometry was used for the results shown in this figure to test for robustness. Fig. 4 shows the result of plane fusion, as described in [18], for the matched planes, followed by projection of the points on the fused plane. The evolution of the robot pose and its uncertainties is shown in Fig. 5. The uncertainties are small but increase cumulatively. This can be avoided by embedding the approach in a SLAM framework, where the overall uncertainty can decrease when certain features (planes) are viewed again in several successive samples.

1) Implementation of Point-to-Point Iterative Closest Point: The P-P ICP algorithm [8], for aligning point clouds, has found wide usage in the 3-D mapping community [6], [9] to estimate robot movement between two successive time instants. For comparison, we have coded our own implementation in C++. The code uses an optimized k -dimensional tree (kd-tree) [37] for fast nearest-neighbor search. The mean-square error e_k at iteration k reduces monotonically with iteration k . The convergence

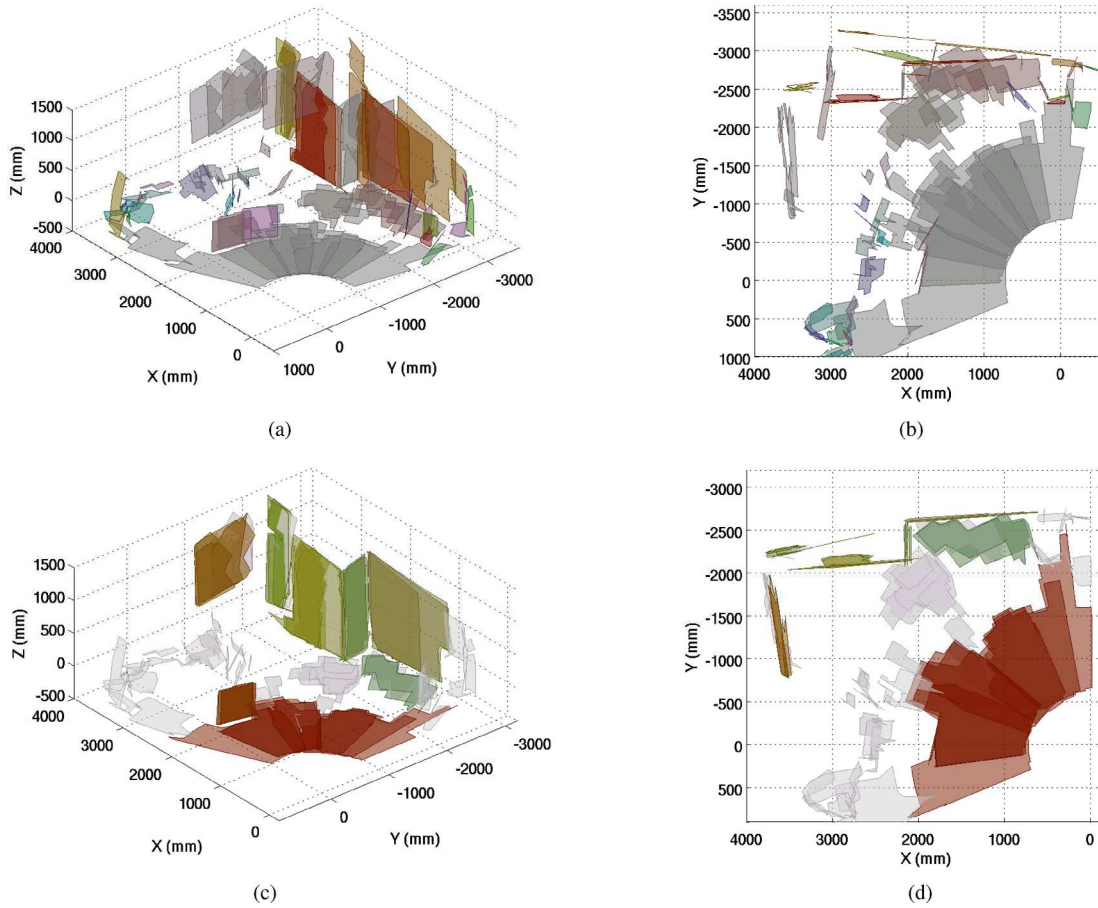


Fig. 3. Results of MUMC for matching planes from the overlapping views from an SR corresponding to Fig. 2(a)–(f). Planes are drawn transparently to show overlap. (a) and (b) Map based on pure odometry. (c) and (d) Result of MUMC algorithm. For the result shown in (c) and (d), as a check, *no odometry was supplied to the MUMC algorithm*. The algorithm aligned most planes properly. [(Front view) (a)] Odometry-based pose estimation with all planes drawn transparently. The plane color is a function of its normal direction and is not related to any matching. [(Top view) (b)] Odometry-based pose estimation with all planes drawn transparently. [(Front view) (c)] Planes matched and aligned using MUMC. Corresponding matched planes are drawn with the same color. Unmatched and filtered-out planes are shown grayed out. [(Top view) (d)] Planes matched and aligned using MUMC. Unmatched and filtered out planes are shown grayed out.

criterion used was $(e_k - e_{k+1})/e_k < 0.0001$, which is independent of the size of the point cloud.

2) *Implementation of Point-to-Plane Iterative Closest Point:* Our implementation of (P-L) ICP [10], [11] uses a kd-tree [37] to find intersection of a line and a surface. A sliding window of size 15×15 is used to estimate *local* normals needed for the algorithm. The cost function [10, Eq. (11)] has no closed-form solution. Therefore, it is minimized using the method of linearization, which is recommended in [10]. The convergence threshold was taken as $\epsilon_e = 10$. Unlike P-P ICP, the convergence of P-L ICP is not monotonic because the number of found correspondences varies across iterations.

3) *Implementation of Three-Dimensional Normal Distribution Transform:* 3-D NDT [5], [38] is a voxel-based approach akin to occupancy grids, except that a probability distribution rather than a single occupancy value is defined for each cell. Magnusson *et al.* [5] have kindly provided us an access to their code, and they have also tuned the parameters of NDT for our datasets. These parameters for the SR dataset were bin spacing 2.0, with iterative split 0.1.

4) *Comparison of Algorithms:* P-P ICP is robust with respect to large perturbations *if the point set itself has not changed*.

However, as Fig. 6 shows, P-P ICP becomes brittle if applied to two successive views with moderate pose change. In the example, it was a rotation of about 12° . This lack of robustness occurs due to the points in one view, which are absent in the other. Fig. 6(a) shows the solution given by the MUMC algorithm, which shows good alignment. Even if we initialize the ICP with this solution, it still converges to the result shown in Fig. 6(b). Thus, the real solution is not even a local minimum with respect to the P-P ICP cost function. In fact, it converges to a wrong solution for all except one of the pairs of view shown in Fig. 2. The exception pair is from Fig. 2(b) and (c), between which the robot does not move, although the odometry says it does, and the only difference in the point clouds is due to the sensor noise.

This lack of robustness is, of course, a function of the FOV and range of the 3-D sensor employed. Higher values of these parameters will effectively increase the pose-difference convergence radius of ICP. Nüchter *et al.* [6] used a servo-operated LRF in a stop-and-go fashion. Their sensor had the FOV of $180^\circ(h) \times 120^\circ(v)$. The range was not mentioned, although the SICK LRF employed is known to have a range of about 30 m. Such a high FOV and range allowed them to take measurements

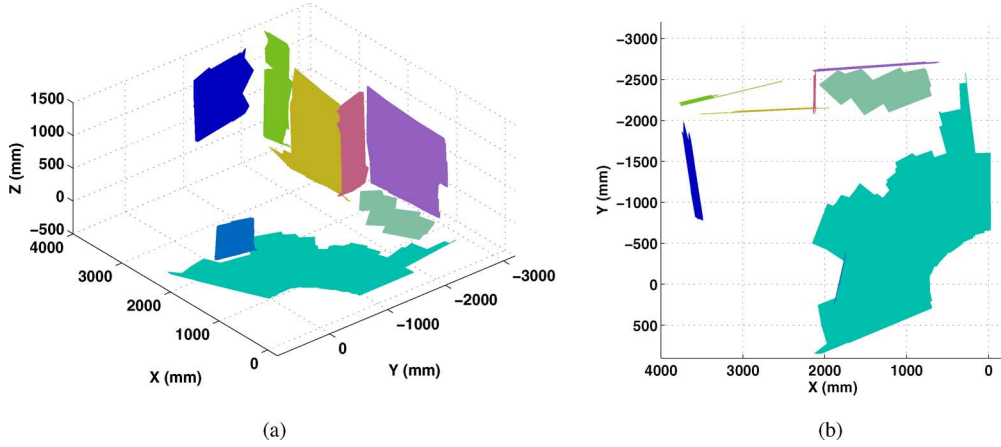


Fig. 4. Result of applying plane fusion based on the methodology described in [18] on the matching results shown in Fig. 3(c) and (d). Rotations were computed using the faster method of Section II-C, which uses isotropic uncertainties. [(Front view) (a)] Fused planes. [(Top view) (b)] Fused planes.

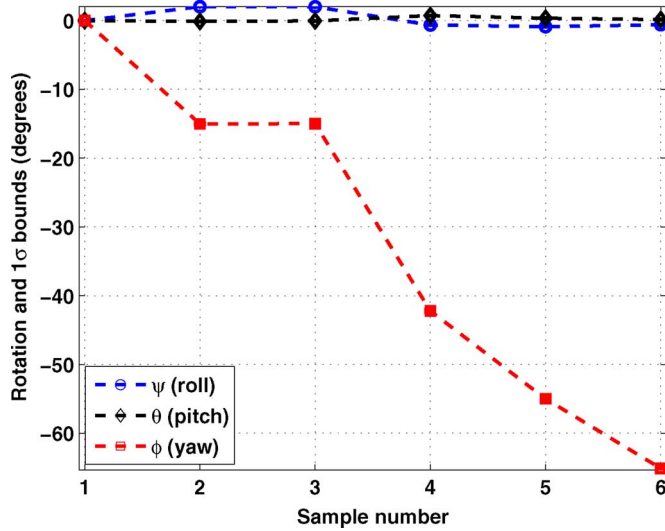


Fig. 5. Computed robot pose and uncertainties for the dataset of Fig. 3. Only rotation is shown because the translation is insignificantly small for this dataset. The rotational uncertainties are too small to be visible in the figure.

every 2.5 m. On the other hand, the SR has a much smaller FOV and range. As shown in Section IV-B, having a sensor with a higher FOV only helps the MUMC algorithm, since, in this case, the number of overlapping planes within successive views increases.

The comparison of computation times is summarized in Table IV. A scan-matching success is marked with \checkmark , failure with \times , and if the matching was only *partially* successful [e.g., see Fig. 6(b), where the rotation is more or less correct], it is marked with a “P.” The heading “100%” in P-P and P-L ICP shows that all the points were taken. The heading “100%” in MUMC is the parameter $F_t\%$ value and shows that all planes were considered in matching. On the other hand, “50%” means that the planes were sorted based on their evidence, and only the top half were considered for matching. The matching results remain unaffected, although the computation time is drastically reduced. For 3-D NDT, 100% of the points are supplied, although due to the grid discretization, the point cloud is effectively compressed.

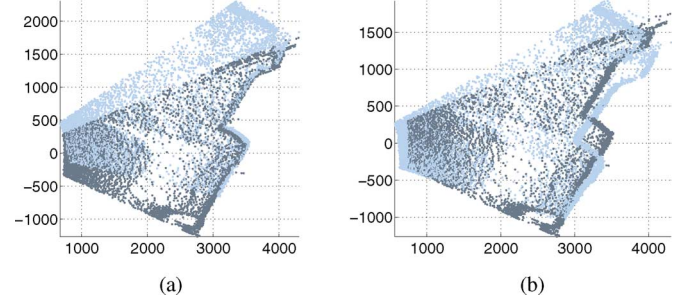


Fig. 6. Registration done using P-P ICP. [Top view] Point-cloud pair corresponding to successive samples of Fig. 2(d) and (e). Point cloud subsampled by 3 for better visualization. (a) Point clouds initialized with the MUMC solution. Note the good alignment. (b) Final convergent solution from initialization using MUMC solution of (a).

As Table IV makes clear, both P-P and P-L ICP can be made faster and more accurate by providing odometry estimates. P-P ICP was overall least successful for this dataset. Both P-L ICP and 3-D NDT were unable to match pair 3, 4 without odometry. In this pair, a predominant plane suddenly goes out of view. By contrast, MUMC was able to process all scan pairs without being provided any odometry or prior estimate. Even if we add the time for plane extraction using region-growing (see Table III) to the time taken by MUMC, it still remains the fastest method among the four. We note that the polygonization step is only required for visualization and that, except for the first pair, the matching of two scans requires the planes extraction by region-growing of only one new scan. The relatively higher time of processing for the first pair by MUMC for the “100%” case is because of the large number (i.e., 39) of patches in the first scan, most of which were of low evidence. The columns with heading # show the number of corresponding pairs found.

We can thus conclude that the MUMC approach is both faster and more robust than both variants of ICP. As compared with 3-D NDT, MUMC is more robust, with a similar computation time when no evidence-based sorting is used. When the planes are sorted based on their evidence and only the top half are considered for matching, the matching results remain unaffected,

TABLE IV

SR DATASET: COMPARISON OF COMPUTATION TIME (IN SECONDS) AND MATCHING SUCCESS FOR DIFFERENT ALGORITHMS. MUMC WAS THE ONLY MATCHER TO SUCCEED FOR ALL PAIRS WITHOUT ODOMETRY. IN ADDITION, IT IS BY FAR THE FASTEST, ESPECIALLY WHEN EVIDENCE BASED SORTING IS USED

Scan Pair	ICP (Point-Point)				ICP (Point-Plane)				3D NDT				MUMC				
	No Odo.		Odometry		No Odo.		Odometry		No Odo.		Odometry		No Odo.				
	100%		100%		100%		100%		100%		100%		100%	#	50%	#	
1,2	7.64	×	1.13	×	19.44	✓	9.78	✓	10.2	✓	11.2	✓	4.781	4	0.493	4	✓
2,3	1.25	✓	2.16	✓	1.43	✓	8.56	✓	5.89	✓	8.77	✓	1.550	9	0.120	6	✓
3,4	5.84	×	0.72	×	42.14	×	60.03	✓	10.5	×	13.4	×	0.318	5	0.042	4	✓
4,5	5.01	×	0.80	P	8.73	✓	3.96	✓	12.1	P	11.3	✓	0.164	6	0.048	6	✓
5,6	13.66	×	3.25	P	16.28	✓	7.83	✓	8.07	✓	12.5	✓	0.613	5	0.096	6	✓



Fig. 7. Intensity images for the first and the last samples taken from [39]. The others can be viewed online. (a) First sample r1_0 in the sequence. (b) Last sample r1_20 in the sequence.

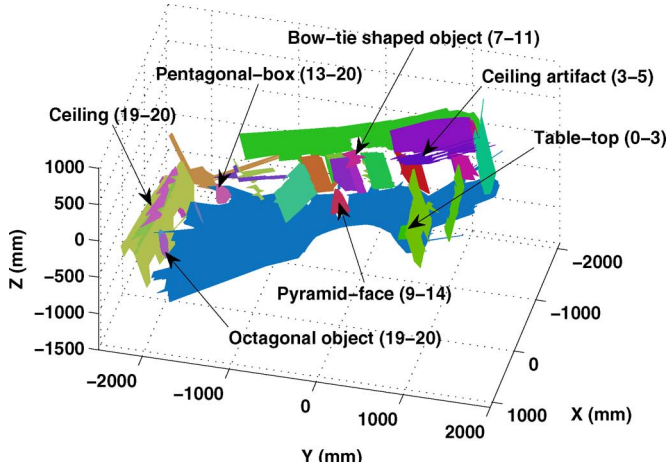


Fig. 8. Annotated front view with final fused planes. Note that even far-away objects were matched and their geometry is recognizable. The number ranges in parenthesis are the view numbers in the dataset in which the object is visible. For intensity images of the views, see [39]. It appears that the LADAR was mounted on the robot tilted downward.

and the computation time for MUMC is drastically reduced, thereby making it, by far, the fastest.

Another major advantage is in terms of storage requirements. A plane summarizes the information from a lot of spatial points. Storing these planes in a graph node in a GraphSLAM-like approach is thus much more storage-efficient than storing the entire point clouds. This continues to be valid, even if we store the polygonized boundaries of the points belonging to a plane, along with the parameters of the infinite plane. The only disadvantage of MUMC is that it requires planar features, i.e., indoors and urban outdoor scenarios, although we also had surprisingly good results in quite unstructured outdoor environments [16].

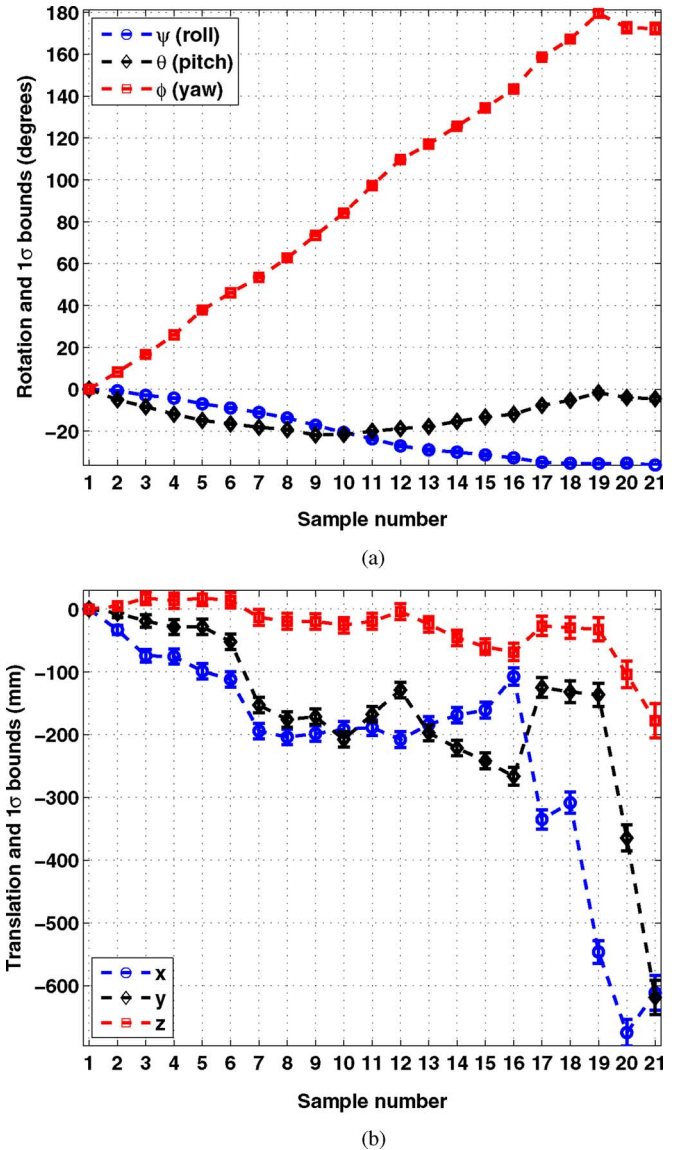


Fig. 9. Results from matching the first 21 views of the USF-Odetics r1 dataset. (a) Computed robot rotation. Sample 1 corresponds to r1_0, which is the zeroth view. (b) Computed robot translation. Sample 1 corresponds to r1_0, which is the zeroth view.

C. University of South Florida Odetics Laser Detection and Ranging Ego-Motion Dataset r1

The USF range image is a popular dataset, which has been online now for more than a decade. We tested our algorithm with the ego-motion data-subset r1 recorded using

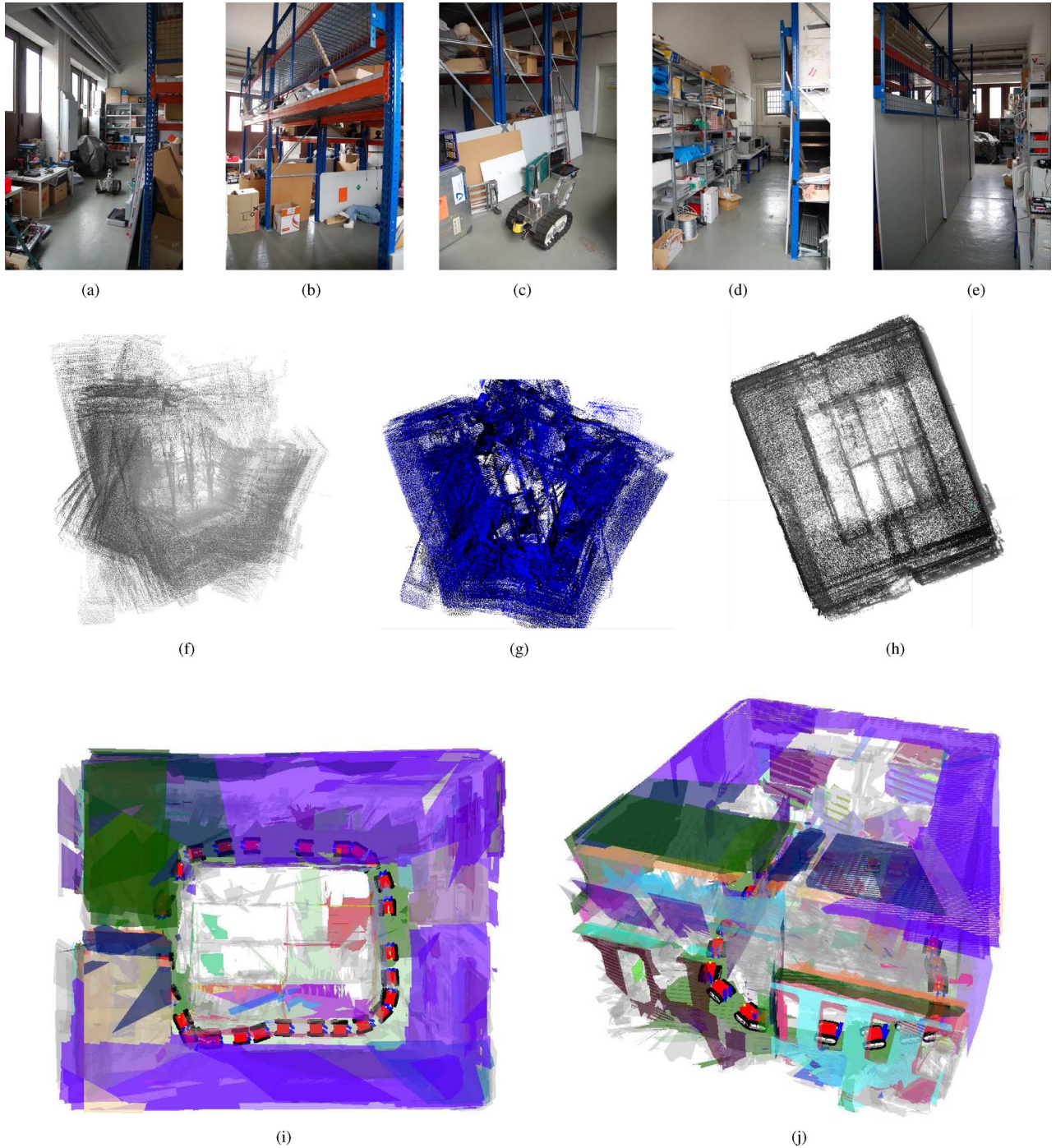


Fig. 10. (a)–(e) Indoor multistory-robot-rescue arena. The robot goes one full round around it. The robot is shown at scan locations in the map (see also Fig. 11). The matched planes are shown in the same semitransparent color, while unmatched planes are grayed out. (f) The top view of the odometry based pointcloud map. The robot starts at upper right. (g) The top view of the point-cloud map created by point-to-plane ICP. (h) The top view of the point-cloud map created by 3D NDT. Unlike in the scenario of Section IV-B, 3D NDT performed better than P-L ICP. (i) The top view of the MUMC map. The robot starts at top left and goes clockwise around. (j) The tilted top view showing the windows in the front which are visible in Fig. 10(a).

the Odetics Laser Detection and Ranging (LADAR) with resolution 128×128 , FOV $60^\circ \times 60^\circ$, and a relatively poor range resolution of 3.66 cm. It is available online at <http://marathon.csee.usf.edu/range/icons/Odet-cam-mot.html> [39] (left dataset; see Fig. 7). The dataset represents a sequence of samples taken from the LADAR mounted on a robot moving in a cluttered lab environment. No odometry or

ground truth is available. It has also been studied in [2, Fig. 17], who provide the result for the registration of only 9 samples (r1_1 to r1_9) out of 40.

The results of MUMC matching for the first 21 successive samples, i.e., r1_0 to r1_20, are shown in Figs. 8 and 9. We have applied the coordinate transform $x \mapsto -x, y \mapsto z, z \mapsto y$ to their point clouds to retain our definition of roll–pitch–yaw



Fig. 11. Inside view of the map of Fig. 10. The robot is shown at scan locations in the map by its 3-D avatar, which is true to scale—for a rough estimation, it can be considered to be a cube of side 0.5 m.

angles. Fig. 9(a) and (b) shows the computed robot-pose change. MUMC reports insufficient overlap for the pair r1_20 to r1_21, which is also obvious to the human eye. Since no odometry is available, the sequence is broken. There are, however, other sequences, which match.

Due to similar resolution, the time for region-growing and polygonization remain similar to that of the SR. The number of planar patches per scan varied between 8 and 19. Since odometry was unavailable, we set $F_t = 100\%$, for which the MUMC matching time per pair varied between 0.1 and 0.66 s.

D. Actuated Laser-Range-Finder Datasets

Finally, we provide some larger examples of data collected using a large FOV sensor, namely, the ALRF. The ALRF provides only range images, but no intensity images. Following two scenarios are considered.

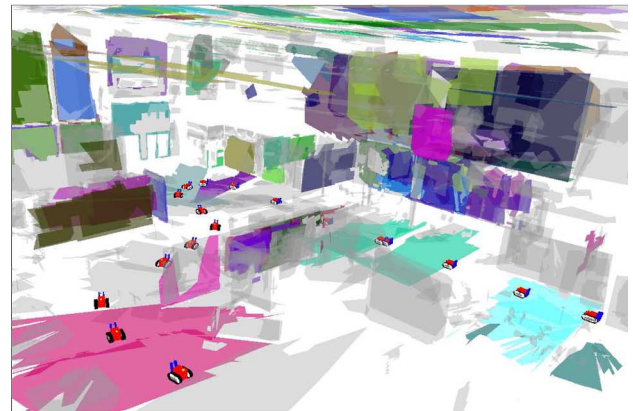
1) *Multistory Robot-Rescue Arena*: The robot was teleoperated to go around the arena, and data were collected in a stop-and-go fashion. A total of 29 scans were taken. Due to the discrete rotations of the actuator pitching the LRF, each scan took about 20 s. The main difficulty in this dataset is the large occlusions when the robot turns a corner.

The arena, its odometry map, its PL ICP map, and different views of its MUMC map are shown in Figs. 10 and 11. Odometry was provided to the algorithms. PL ICP fully succeeded in 53.6% of pairs, partially succeeded in 35.7% of pairs, and failed for 10.7% of pairs. P-P ICP was, as expected, less robust than PL ICP. It succeeded in only about 30% of pairs, partially succeeded in 35%, and failed in 35% of cases. 3-D NDT performed much better than P-L ICP for this scenario than in the SR scenario of Section IV-B. In both cases, its parameters were tuned by its designers [5].

The plane-fitting time per scan was on an average 3 s, and MUMC took about 0.8 s on average for matching a scan-pair for $F_t = 15\%$. Another 3 s is required for polygonizations of planar patches for visualization. The accuracy of the scan matching can be seen by the fact that there is hardly any rotation or translation error present when the loop is closed and the robot returns



(a)



(b)

Fig. 12. Hannover Fair German Robocup 2009 hall and its map created using MUMC. No odometry was provided to the algorithm. Note the relatively large area covered compared with the size of the robot. (a) View of the hall. (b) Tilted top view from below the ceiling.

near its starting location. Thus, the map is already quite self-consistent even without any relaxation step.

2) *Hannover Fair German Robocup 2009 Hall*: Data were collected as before, except that the robot movements between scans were large: sometimes up to 5 m in translation and 55° in rotation. No odometry was available. Due to these constraints, more conservative size-similarity and overlap parameters had to be taken, viz., $\bar{L}_{det} = 7$, and $\bar{\chi}_{ovlp}^2 = 1.25$, although $F_t = 20\%$ as before. The resulting map is shown in Fig. 12.

3) *Other Datasets and Multimedia*: Further datasets, including a quite unstructured outdoor scenario at Disaster City, are available at <http://robotics.jacobs-university.de/projects/3Dmap/>. Multimedia of all 3-D maps are also provided there.

V. CONCLUSION

The mathematical machinery for doing online pose registration, which are based solely on planes extracted from range images, was presented. First, the simpler case of known plane correspondences was tackled. We derived expressions for LSs pose and its covariance estimation considering plane-parameter uncertainty. Then, the work is extended to the general case by

introducing a new algorithm to determine the unknown plane correspondences. This is done by maximizing geometric consistency. In doing so, a very efficient way to search the space of possible correspondences was introduced. To supplement the theoretical results, experiments for three 3-D sensors were presented. Compared with ICP and 3-D NDT, the presented algorithm is shown to be faster, to have a bigger convergence radius, and to require less memory.

APPENDIX A

LEAST-SQUARES PLANE FITTING

The planar patches are first extracted from a given range image from a 3-D sensor using a region-growing algorithm, as described in [17]. The uncertainty analysis of the plane-extraction process is given in [18] and summarized here. Let us assume that a planar patch has been extracted, and is known to be composed of a set of points \mathbf{p}_j , $j = 1, \dots, N$. Their covariances $\mathbf{C}_{\mathbf{p},j}$, which are usually taken to be linear or quadratic functions of their respective $\|\mathbf{p}_j\|$, are also known. The weights and the weighted center of mass for these points is given by

$$w_j^{-1} \triangleq \text{trace}(\mathbf{C}_{\mathbf{p},j}) \quad (47)$$

$$\mathbf{p}_c \triangleq \frac{\sum_{j=1}^N w_j \mathbf{p}_j}{\sum_{j=1}^N w_j}, \quad \mathbf{C}_{\mathbf{p}_c} = \left(\sum_{j=1}^N w_j \right)^{-1} \mathbf{I}. \quad (48)$$

The very same weights have also been employed in [9]. Then, the LSs plane parameters are determined as follows:

$$\mathbf{M} \triangleq \sum_{j=1}^N w_j (\mathbf{p}_j - \mathbf{p}_c)(\mathbf{p}_j - \mathbf{p}_c)^\top. \quad (49)$$

The plane normal $\hat{\mathbf{n}}$ is the eigenvector of \mathbf{M} corresponding to its minimum eigenvalue. The plane parameter $d = \hat{\mathbf{n}}^\top \mathbf{p}_c$, as the plane passes through \mathbf{p}_c . The covariance of the plane parameters is $\mathbf{C} = -\mathbf{H}^+$, where the Hessian matrix \mathbf{H} is defined as

$$\mathbf{H} = \begin{bmatrix} \mathbf{H}_{\hat{\mathbf{n}}\hat{\mathbf{n}}} & \mathbf{H}_{\hat{\mathbf{n}}d} \\ \mathbf{H}_{\hat{\mathbf{n}}d}^\top & \mathbf{H}_{dd} \end{bmatrix} \quad (50a)$$

where

$$\mathbf{H}_{dd} = -\sum_{j=1}^N w_j, \quad \mathbf{H}_{\hat{\mathbf{n}}d} = -\mathbf{H}_{dd} \mathbf{p}_c \quad (50b)$$

$$\mathbf{H}_{\hat{\mathbf{n}}\hat{\mathbf{n}}} = -\mathbf{M} + \mathbf{H}_{dd} \mathbf{p}_c \mathbf{p}_c^\top + (\hat{\mathbf{n}}^\top \mathbf{M} \hat{\mathbf{n}}) \mathbf{I}_3. \quad (50c)$$

From these expressions, it can be derived that

$$\mathbf{H} \begin{bmatrix} \hat{\mathbf{n}} \\ d \end{bmatrix} = \mathbf{0} \Rightarrow \mathbf{C} \begin{bmatrix} \hat{\mathbf{n}} \\ d \end{bmatrix} = \mathbf{0}. \quad (51)$$

APPENDIX B

DECOUPLING THE COVARIANCES

To be able to use the nicely decoupled equations [see (4)] to determine rotation and translation separately, we need to estimate the total uncertainty in $\hat{\mathbf{n}}$ by marginalizing, i.e., integrating

out the effect of d and *vice versa*. Standard results for marginalization of Gaussians are not directly applicable because they are written in terms of the covariance matrix and not the Hessian; the latter is what is directly estimated [18], and the former is computed from it by Moore–Penrose inverse. We show that the marginalization can still be easily performed, if we start from first principles.

Let $\bar{\nu} \triangleq (\bar{\mathbf{n}}^\top, \bar{d})^\top$ be the mean plane parameters and we define the perturbations about the mean as

$$\Delta\nu \triangleq \begin{bmatrix} \Delta\hat{\mathbf{n}} \\ \Delta d \end{bmatrix} \triangleq \begin{bmatrix} \hat{\mathbf{n}} - \bar{\mathbf{n}} \\ d - \bar{d} \end{bmatrix}. \quad (52)$$

The corresponding joint probability-distribution function (PDF) is given in terms of the plane's Hessian \mathbf{H} as

$$p(\nu | \bar{\nu}, \mathbf{H}) = \eta \exp \left\{ \frac{1}{2} \Delta\nu^\top \begin{bmatrix} \mathbf{H}_{\hat{\mathbf{n}}\hat{\mathbf{n}}} & \mathbf{H}_{\hat{\mathbf{n}}d} \\ \mathbf{H}_{\hat{\mathbf{n}}d}^\top & \mathbf{H}_{dd} \end{bmatrix} \Delta\nu \right\} \quad (53)$$

where η is the normalizing constant, and the Hessian has been written in a partitioned form in the exponent. This PDF is defined on the tangent plane of the domain of ν at $\bar{\nu}$, which implies that

$$(\Delta\hat{\mathbf{n}}) \cdot \bar{\mathbf{n}} \approx 0. \quad (54)$$

From the first of (51) it can be deduced that

$$\mathbf{H}_{dd} - \mathbf{H}_{\hat{\mathbf{n}}d}^\top \mathbf{H}_{\hat{\mathbf{n}}\hat{\mathbf{n}}}^{-1} \mathbf{H}_{\hat{\mathbf{n}}d} = 0. \quad (55)$$

Using this, we can algebraically decompose the exponent of the joint PDF by the method of completion of squares as

$$\Delta\nu^\top \mathbf{H} \Delta\nu = \xi^\top \mathbf{H}_{\hat{\mathbf{n}}\hat{\mathbf{n}}} \xi, \quad \xi \triangleq \Delta\hat{\mathbf{n}} + \Delta d \mathbf{H}_{\hat{\mathbf{n}}\hat{\mathbf{n}}}^{-1} \mathbf{H}_{\hat{\mathbf{n}}d} \quad (56)$$

which shows that the random variable $\xi \in \mathbb{R}^3$ is normally distributed with mean $\mathbf{0}$ and covariance $-\mathbf{H}_{\hat{\mathbf{n}}\hat{\mathbf{n}}}^{-1}$. Taking the component of ξ along $\bar{\mathbf{n}}$ and using (54) gives

$$\bar{\mathbf{n}}^\top \xi = \Delta d \bar{\mathbf{n}}^\top \mathbf{H}_{\hat{\mathbf{n}}\hat{\mathbf{n}}}^{-1} \mathbf{H}_{\hat{\mathbf{n}}d}. \quad (57)$$

This finally allows us to derive the decoupled covariance of Δd as

$$\mathbf{D}_{dd} = \frac{-\bar{\mathbf{n}}^\top \mathbf{H}_{\hat{\mathbf{n}}\hat{\mathbf{n}}}^{-1} \bar{\mathbf{n}}}{(\bar{\mathbf{n}}^\top \mathbf{H}_{\hat{\mathbf{n}}\hat{\mathbf{n}}}^{-1} \mathbf{H}_{\hat{\mathbf{n}}d})^2}. \quad (58)$$

To compute the decoupled covariance of $\Delta\hat{\mathbf{n}}$, we decompose the exponent of the joint PDF again by method of completion of squares as

$$\Delta\nu^\top \mathbf{H} \Delta\nu = \Delta\hat{\mathbf{n}}^\top (\mathbf{H}_{\hat{\mathbf{n}}\hat{\mathbf{n}}} - \mathbf{H}_{\hat{\mathbf{n}}d} \mathbf{H}_{dd}^{-1} \mathbf{H}_{\hat{\mathbf{n}}d}^\top) \Delta\hat{\mathbf{n}} + \mathbf{H}_{dd} (\Delta d + \mathbf{H}_{dd}^{-1} \mathbf{H}_{\hat{\mathbf{n}}d}^\top \Delta\hat{\mathbf{n}})^2. \quad (59)$$

This decomposition can be used to integrate out Δd from the joint PDF, and we get the decoupled Hessian for $\Delta\hat{\mathbf{n}}$ as

$$\mathbf{H}'_{\hat{\mathbf{n}}\hat{\mathbf{n}}} \triangleq \mathbf{H}_{\hat{\mathbf{n}}\hat{\mathbf{n}}} - \mathbf{H}_{\hat{\mathbf{n}}d} \mathbf{H}_{dd}^{-1} \mathbf{H}_{\hat{\mathbf{n}}d}^\top. \quad (60)$$

Using (51), it can be verified that we have the nice property $\mathbf{H}'_{\hat{\mathbf{n}}\hat{\mathbf{n}}} \bar{\mathbf{n}} = \mathbf{0}$. Finally, the decoupled covariance of $\Delta\hat{\mathbf{n}}$ is given by

$$\mathbf{D}_{\hat{\mathbf{n}}\hat{\mathbf{n}}} \triangleq -(\mathbf{H}'_{\hat{\mathbf{n}}\hat{\mathbf{n}}})^+, \quad \mathbf{D}_{\hat{\mathbf{n}}\hat{\mathbf{n}}} \bar{\mathbf{n}} = \mathbf{0}. \quad (61)$$

REFERENCES

- [1] H. Durrant-Whyte and T. Bailey, "Simultaneous localization and mapping: Part I," *IEEE Robot. Autom. Mag.*, vol. 13, no. 2, pp. 99–108, Jun. 2006.
- [2] D. Fischer and P. Kohlhepp, "3D geometry reconstruction from multiple segmented surface descriptions using neuro-fuzzy similarity measures," *J. Intell. Robot. Syst.*, vol. 29, pp. 389–431, 2000.
- [3] H. Surmann, A. Nüchter, and J. Hertzberg, "An autonomous mobile robot with a 3D laser range finder for 3D exploration and digitalization of indoor environments," *Robot. Auton. Syst.*, vol. 45, no. 3/4, pp. 181–198, 2003.
- [4] J. Weingarten and R. Siegwart, "3D SLAM using planar segments," in *Proc. IEEE/RSJ Int. Conf. Intell. Robots Syst.*, Beijing, China, 2006, pp. 3062–3067.
- [5] M. Magnusson, A. Lilienthal, and T. Duckett, "Scan registration for autonomous mining vehicles using 3D-NDT," *J. Field Robot.*, vol. 24, no. 10, pp. 803–827, 2007.
- [6] A. Nüchter, K. Lingemann, and J. Hertzberg, "6D SLAM—3D mapping outdoor environments," *J. Field Robot.*, vol. 24, no. 8/9, pp. 699–722, 2007.
- [7] CSEM. (2006). *The SwissRanger, manual V1.02*. CSEM, Zurich, Switzerland [Online]. Available: <http://www.swissranger.ch>
- [8] P. J. Besl and N. D. McKay, "A method for registration of 3-d shapes," *IEEE Trans. Pattern Anal. Mach. Intell.*, vol. 14, no. 2, pp. 239–256, Feb. 1992.
- [9] J. Weingarten. (2006). "Feature-based 3D SLAM," Ph.D. dissertation, EPFL, Lausanne, Switzerland [Online]. Available: <http://library.epfl.ch/theses/?nr=3601>
- [10] Y. Chen and G. Medioni, "Object modeling by registration of multiple range images," in *Proc. IEEE Int. Conf. Robot. Autom.*, 1991, vol. 3, pp. 2724–2729.
- [11] Y. Chen and G. Medioni, "Object modeling by registration of multiple range images," *Image Vis. Comput.*, vol. 10, no. 3, pp. 145–155, 1992.
- [12] M. W. M. G. Dissanayake, P. Newman, S. Clark, and H. F. Durrant-Whyte, "A solution to the simultaneous localization and map building (SLAM) problem," *IEEE Trans. Robot. Autom.*, vol. 17, no. 3, pp. 229–241, Jun. 2001.
- [13] B. K. P. Horn and J. G. Harris, "Rigid body motion from range image sequences," *CVGIP: Image Understanding*, vol. 53, pp. 1–13, 1991.
- [14] H. Gharavi and S. Gao, "3-D motion estimation using range data," *IEEE Trans. Intell. Transp. Syst.*, vol. 8, no. 1, pp. 133–143, Mar. 2007.
- [15] O. D. Faugeras and F. Lustman, "Motion and structure from motion in piecewise planar environment," *Int. J. Pattern Recogn. Artif. Intell.*, vol. 2, no. 3, pp. 485–508, 1988.
- [16] K. Pathak, A. Birk, N. Vaskevicius, M. Pfingsthorn, S. Schwertfeger, and J. Poppinga, "Online three-dimensional SLAM by registration of large planar surface segments and closed-form pose-graph relaxation," *J. Field Robot.*, vol. 27, no. 1, pp. 52–84, 2010.
- [17] J. Poppinga, N. Vaskevicius, A. Birk, and K. Pathak, "Fast plane detection and polygonalization in noisy 3D range images," in *Proc. IEEE Int. Conf. Intell. Robots Syst.*, Nice, France, 2008, pp. 3378–3383.
- [18] K. Pathak, N. Vaskevicius, and A. Birk, "Uncertainty analysis for optimum plane extraction from noisy 3D range-sensor point-clouds," *Intell. Serv. Robot.*, vol. 3, pp. 37–48, 2010.
- [19] P. Kohlhepp, P. Pozzo, M. Walther, and R. Dillmann, "Sequential 3D-SLAM for mobile action planning," in *Proc. IEEE/RSJ Int. Conf. Intell. Robots Syst.*, Sep./Oct., 2004, vol. 1, pp. 722–729.
- [20] P. Kohlhepp, G. Bretthauer, M. Walther, and R. Dillmann, "Using orthogonal surface directions for autonomous 3d-exploration of indoor environments," in *Proc. IEEE/RSJ Int. Conf. Intell. Robots Syst.*, Oct. 2006, pp. 3086–3092.
- [21] R. Fisher, "Geometric constraints from planar surface patch matching," *Image Vis. Comput.*, vol. 8, no. 2, pp. 148–154, 1990.
- [22] W. E. L. Grimson, *Object Recognition by Computer: The Role of Geometric Constraints*. Cambridge, MA: MIT Press, 1990.
- [23] W. He, W. Ma, and H. Zha, "Automatic registration of range images based on correspondence of complete plane patches," in *Proc. 5th Int. Conf. 3-D Dig. Imag. Modeling*, Piscataway, NJ: IEEE, 2005, pp. 470–475.
- [24] D. Viejo and M. Cazorla, "3D plane-based egomotion for SLAM on semi-structured environment," in *Proc. IEEE/RSJ Int. Conf. Intell. Robots Syst.*, 2007, pp. 2761–2766.
- [25] A. Makadia, A. Patterson, and K. Daniilidis, "Fully automatic registration of 3D point clouds," in *Proc. IEEE Comp. Soc. Conf. Comput. Vis. Pattern Recogn.*, Jun. 2006, vol. 1, pp. 1297–1304.
- [26] M. A. Fischler and R. C. Bolles, "Random sample consensus: A paradigm for model fitting with applications to image analysis and automated cartography," *Graph. Image Process.*, vol. 24, no. 6, pp. 381–395, 1981.
- [27] D. Fontannelli, L. Ricciato, and S. Soatto, "A fast RANSAC-based registration algorithm for accurate localization in unknown environments using LIDAR measurements," in *Proc. IEEE Int. Conf. Autom. Sci. Eng.*, 2007, pp. 597–602.
- [28] J. J. Craig, *Introduction to Robotics—Mechanics and Control*. 3rd ed. Englewood Cliffs, NJ: Prentice-Hall, 2005.
- [29] Y. Kanazawa and K. Kanatani, "Reliability of fitting a plane to range data," *IEICE Trans. Inf. Syst.*, vol. E78-D, no. 12, pp. 1630–1635, 1995.
- [30] K. Kanatani, *Statistical Optimization for Geometric Computation*. New York: Dover, 2005. ISBN: 0486443086
- [31] D. S. Sivia, *Data Analysis: A Bayesian Tutorial*. Oxford, U.K.: Oxford Univ. Press, 1996.
- [32] B. K. P. Horn, "Closed-form solution of absolute orientation using unit quaternions," *J. Opt. Soc. Amer. A*, vol. 4, pp. 629–642, 1987.
- [33] M. D. Shuster, "The generalized Wahba problem," *J. Astronaut. Sci.*, vol. 54, no. 2, pp. 245–259, Apr.–Jun. 2006.
- [34] F. L. Markley, "Attitude estimation or quaternion estimation?" presented at the Flight Mech. Symp., Greenbelt, MD, 2003.
- [35] A. Carmi and Y. Oshman, "On the covariance singularity of quaternion estimators," presented at the AIAA Guid., Navigat. Control Conf. Exhibit, Hilton Head, SC, 2007.
- [36] G. H. Golub and C. F. V. Loan, "An analysis of the total least squares problem," *SIAM J. Numer. Anal.*, vol. 17, no. 6, pp. 883–893, 1980.
- [37] D. M. Mount and S. Arya. (2006). *ANN: A library for approximate nearest neighbor searching* [Online]. Available: <http://www.cs.umd.edu/~mount/ANN/>
- [38] M. Magnusson, A. Nüchter, C. Lörken, A. J. Lilienthal, and J. Hertzberg, "Evaluation of 3d registration reliability and speed a comparison of ICP and NDT," in *Proc. IEEE Int. Conf. Robot. Autom.*, Kobe, Japan, 2009, pp. 3907–3912.
- [39] A. Hoover. (1994). *Ego-motion sequence using Odetics LADAR r1* [Online]. Available: <http://marathon.csee.usf.edu/range/icons/Odet-cam-mot.html>



Kaustubh Pathak (S'03–M'05) received the Ph.D. degree in mechanical engineering (nonlinear control of underactuated and nonholonomic systems) from the University of Delaware, Newark, in the Fall of 2005.

Since 2006, he has been a Postdoctoral Fellow with the Robotics Group, Department of Electrical Engineering and Computer Science, Jacobs University Bremen, Bremen, Germany. He has authored or coauthored more than 35 papers in international journals and conferences. His current research interests include probabilistic feature extraction and fusion, three-dimensional (3-D) mapping, path planning, and the control of mobile robots.



Andreas Birk (M'99) received the Doctorate degree from the Universität des Saarlandes, Saarbrücken, Germany, in 1995.

In Fall 2001, he joined Jacobs University Bremen, Bremen, Germany, where he is currently an Associate Professor with the Department Electrical Engineering and Computer Science. He developed a Robotics Group at Jacobs University Bremen. He was a Research Mandate with the Flemish Society for Applied Research and a Visiting Professor with the Vrije Universiteit Brussel, Brussels, Belgium, where he was engaged in research with the Artificial Intelligence Laboratory. His current research interests include autonomous systems. On the engineering side, he is involved in the design and construction of complete systems, which includes the design and construction of embedded hardware and mechatronics, as well as software development up to full autonomy. On the basic research side, he is engaged in a constructive understanding of intelligence.



robotics (SSRR).

Narūnas Vaškevičius received the M.Sc. degree in computer science in 2008 with robotics specialization from Jacobs University Bremen, Bremen, Germany, where he is currently working toward the Ph.D. degree in computer science with the Jacobs Robotics Laboratory.

His current research interests include autonomous robotics in the context of path planning and 3-D mapping based on probabilistic surface-feature extraction, and the fields of space and underwater robotics, as well as safety, security, and rescue



Jann Poppinga received the Diploma (M.Sc. equivalent) degree in computer science from the University of Oldenburg, Oldenburg, Germany, in 2006. He is currently working toward the Ph.D. degree with Jacobs University Bremen, Bremen, Germany.

He has authored or coauthored four publications. His research interests include 3-D data processing, especially 3-D path planning and mapping for mobile robots.